Proper orthogonal decomposition assisted subfilter-scale model of turbulence for large eddy simulation

Vilas Shinde*
Department of Mechanical and Aerospace Engineering, The Ohio State University, Columbus, Ohio 43210, USA

(Received 20 February 2019; published 31 January 2020; corrected 27 March 2020)

In large eddy simulations (LESs), the large scales of turbulent motion are resolved directly, whereas the small scales that are computationally expensive to solve are modeled. The scale separation is performed either in the physical domain (space or time) or in Fourier space, which involves application of an explicit or implicit scale filtering operation, parting the resolved and subfilter-scales (well known as subgrid scales). Proper orthogonal decomposition (POD) of a turbulent flow also leads to the scale separation, where the POD modes represent characteristic scales of motion. In the present work, the similarity between the physical and Fourier scales and the POD modes, in terms of their kinetic-energy content and the interchange of energy among the scales and modes, is used to model the effect of subfilter-scales of motion for the LES. The subfilter-scales stress tensors, namely, Leonard, cross, and Reynolds are expressed directly in terms of the POD modes, while the cross and Reynolds subfilter-scale stresses are modeled, incorporating the energy contribution of the subfilter-scale POD modes. In addition to the mathematical properties of the subfilter-scale stress tensor, the model inherently predicts the near-wall asymptotic behavior and the backward transfer of subfilter-scale energy (the backscatter).

DOI: 10.1103/PhysRevFluids.5.014605

I. INTRODUCTION

Turbulent flows consist of a wide range of scales of motion, also known as eddies. In the direct numerical simulation (DNS) of the governing flow equations, the Navier-Stokes equations, all the eddies are resolved by means of a very fine numerical grid, leading to computationally very expensive simulations. The cost of the DNS further depends on the scale separation, i.e., the ratio between the most and least energetic eddies, which is typically very large for the flows of practical interest (e.g., external aerodynamics), making DNS intractable for such flows. In large eddy simulations (LESs), the most energetic large eddies are directly computed, whereas the contribution of smaller eddies is modeled in order to lower the computational cost. Thus separation of the large scales from the small scales is an important first step of the LES.

A filtering operation decomposes an instantaneous flow field into the large scales, referred to here as "resolved" scales, and the small scales, referred here as "subfilter" scales. Let $\varphi(\boldsymbol{x}, t)$ be a spacetime variable, where $\boldsymbol{x}$ is three-dimensional space and t is time. The spatial filtering operation on $\varphi(\boldsymbol{x}, t)$ by a convolution kernel G gives the resolved part of the variable as

$$\overline{\varphi}(\boldsymbol{x}, t) = \int_{-\infty}^{\infty} \varphi(\boldsymbol{x} - \boldsymbol{r}, t) G(\boldsymbol{r}, \Delta_{\boldsymbol{x}}) d\boldsymbol{r}, \tag{1}$$

*shinde.33@osu.edu

whereas the subfilter component, denoted by $\varphi''(\boldsymbol{x}, t)$, can be obtained as

$$\varphi''(\boldsymbol{x}, t) = \varphi(\boldsymbol{x}, t) - \overline{\varphi}(\boldsymbol{x}, t). \tag{2}$$

The overline $\bar{\cdot}$ represents a filtered variable. A cutoff length scale, $\Delta_{\boldsymbol{x}}$, is associated with the filter kernel G, which is assumed to be isotropic and uniform, at this point. Furthermore, G satisfies the following three conditions in order to apply the kernel to the Navier-Stokes equations: normalization, linearity, and commutation with differentiation. The normalization ensures that the integral of the kernel is unity, the commutation with derivative ensures that the filtering and derivative operations commute, whereas the product of convolution automatically satisfies the linearity irrespective of the definition of kernel G. The most commonly used filters are the box or top hat filter, Gaussian filter, and sharp spectral filter. For instance, the kernel of the simplest top hat filter, with a cutoff length of $\Delta_{\boldsymbol{x}}$, is given as

$$G(\boldsymbol{r}, \Delta_{\boldsymbol{x}}) = \begin{cases} \frac{1}{\Delta_x} & \text{if } |\boldsymbol{r}| \leqslant \frac{\Delta_x}{2} \\ 0 & \text{otherwise.} \end{cases} \tag{3}$$

It is local in physical space and nonlocal in spectral space, contrary to the sharp spectral filter, which is local in spectral space and nonlocal in physical space. The Gaussian filter however, is nonlocal in both physical and spectral space. The top hat and Gaussian filters are positive with their kernels $G(\boldsymbol{r}) > 0$.

The governing flow equations for the resolved flow can be obtained by applying the filtering operation to the Navier-Stokes equations. At this point, the filter is assumed to be spatially uniform, such that it commutes with the differentiation operation; later in the text (Sec. III), the effect of a nonuniform filter is briefly described. The filtered mass and momentum conservation equations, in an incompressible Cartesian form using index notation, are

$$\frac{\partial \overline{u_i}}{\partial x_i} = 0, \tag{4}$$

$$\frac{\partial \overline{u_i}}{\partial t} + \frac{\partial \overline{u_i}\,\overline{u_j}}{\partial x_j} = -\frac{1}{\rho}\frac{\partial \overline{p}}{\partial x_j} + \nu \frac{\partial^2 \overline{u_i}}{\partial x_i \partial x_j} - \frac{\partial \tau_{ij}}{\partial x_j}, \tag{5}$$

where u_i and p are the velocity components and static pressure. ρ and ν denote the density and kinematic viscosity, respectively. The additional term of τ_{ij} arises due the difference between the filtered product and product of the filtered velocity in the nonlinear term [the second term of Eq. (5)], which comprise the nonlinear triad interactions between the scales [1]. τ_{ij} is the subfilter-scale stress tensor given by

$$\tau_{ij} = \overline{u_i u_j} - \overline{u_i}\,\overline{u_j}. \tag{6}$$

Leonard [2] expressed the subfilter-scale stress in three components as

$$\tau_{ij} = \mathcal{L}_{ij} + \mathcal{C}_{ij} + \mathcal{R}_{ij}. \tag{7}$$

The term $\mathcal{L}_{ij}$ is called Leonard subfilter-scale tensor and represents the interactions among the resolved scales. It is expressed as

$$\mathcal{L}_{ij} = \overline{\overline{u_i}\,\overline{u_j}} - \overline{\overline{u_i}}\,\overline{\overline{u_j}}. \tag{8}$$

The second term, $\mathcal{C}_{ij}$, represents interactions between the large resolved scales and the small subfilter scales; thus it is called the cross tensor [3] and is given by

$$\mathcal{C}_{ij} = \overline{\overline{u_i}u_j''} + \overline{u_i''\overline{u_j}} - \overline{\overline{u_i}u_j''} - \overline{u_i''\overline{u_j}}. \tag{9}$$

Lastly, the term $\mathcal{R}_{ij}$ represents the interaction among the small subfilter scales, similar to the Reynolds stress tensor, and it is expressed as

$$\mathcal{R}_{ij} = \overline{u_i'' u_j''} - \overline{u_i''}\,\overline{u_j''}. \tag{10}$$

The Leonard decomposition of Eq. (7) is also preferred for its Galilean-invariant property [4], even though the individual stresses $(\mathcal{L}_{ij}, \mathcal{C}_{ij})$ are not Galilean invariant [5]. The subfilter-scale stress tensor τ_{ij} is realizable or positive semidefinite if the filter kernel G of Eq. (1) is positive, which is a necessary and sufficient condition [6]. The top hat and Gaussian filters satisfy this condition, leading to a realizable subfilter-scale stress tensor. From a theoretical point of view, modeling of the subfilter-scale stress tensor must retain its basic properties, including the tensor symmetry, Galilean invariance and realizability. Such a requirement is also based on practical aspects such as the numerical stability [7].

In the governing equations of LES [Eqs. (4) and (5)], the subfilter-scale stress tensor τ_{ij} must be modeled accurately in order to represent the effects of subfilter scales on the resolved scale dynamics. An important aspect modeling the subfilter-scale stress tensor is the transfer of kinetic energy between the resolved and subfilter scales. In a fully developed isotropic turbulence, the transfer of energy occurs from the resolved scales to the subfilter scales, the mechanism is known as forward cascade of energy; whereas energy transfer from subfilter scales to resolved scales is known as backward cascade or backscatter of energy [8,9]. On average, the forward transfer of energy from resolved scales to subfilter scales is the main phenomenon [10]. The simplest model for forward energy transfer has been proposed by Smagorinsky [11], which assumes that the effect of subfilter scales on resolved scales is analogous to molecular diffusion; thus it is modeled in terms of the subfilter-scale viscosity ν_{sfs}, similar to the Boussinesq eddy-viscosity assumption. The trace-free subfilter-scale stress tensor is expressed as

$$\tau_{ij} - \tfrac{1}{3}\tau_{kk}\delta_{ij} = -2\nu_{sfs}\overline{S}_{ij}, \tag{11}$$

where $\overline{S}_{ij}$ is the resolved rate-of-strain tensor defined as

$$\overline{S}_{ij} = \frac{1}{2}\left(\frac{\partial \overline{u}_i}{\partial x_j} + \frac{\partial \overline{u}_j}{\partial x_i}\right). \tag{12}$$

The subfilter-scale viscosity is modeled by using the mixing-length analogy as

$$\nu_{sfs} = (C_s\Delta_{\boldsymbol{x}})^2|\overline{S}|, \quad \text{where } |\overline{S}| = (2\overline{S}_{ij}\overline{S}_{ij})^{\frac{1}{2}}. \tag{13}$$

The derivation of the Smagorinsky model is based on Kolmogorov's theory of isotropic turbulence [12]. The filter cutoff length expected to lie in the inertial subrange, where the energy spectra exhibit the $k^{-5/3}$ power law, and the kinetic energy is only transferred from the large scales to the small scales of turbulence. The theoretical value of the proportionality coefficient C_s, also Smagorinsky coefficient, is $\sim$0.18, whereas the filter cutoff length $\Delta_{\boldsymbol{x}}$ is analogous to the mixing-length. The value of the Smagorinsky coefficient is not universal and should change with the flow regimes and configurations [13–15]; particularly, it should attenuate near a wall and become zero for laminar flows.

Germano *et al.* [16] proposed a dynamic procedure to obtain locally varying values of the Smagorinsky coefficient. In the dynamic procedure, the filtering operation is performed two times. Let $\widetilde{\cdot}$ denote the second filter of a larger size $\tilde{\Delta}_{\boldsymbol{x}}$. The resolved stress tensor is then given as

$$L_{ij} = \widetilde{\overline{u}_i\overline{u}_j} - \widetilde{\overline{u}}_i\widetilde{\overline{u}}_j, \tag{14}$$

which is also known as the Germano identity. It represents an additional contribution to the subfilter-scale stress due to the second filter of larger cutoff length. For the dynamic procedure, an expression for the Smagorinsky coefficient C_s that best complies with the Germano identity is proposed by Lilly [17]:

$$C_s^2 = \frac{\langle M_{ij}L_{ij}\rangle}{\langle M_{kl}M_{kl}\rangle}, \tag{15}$$

where

$$M_{ij} = 2\Delta_{\boldsymbol{x}}^2\widetilde{|\overline{S}|\overline{S}_{ij}} - 2\tilde{\Delta}_{\boldsymbol{x}}^2|\widetilde{\overline{S}}|\widetilde{\overline{S}}_{ij}. \tag{16}$$

The brackets $\langle\cdot\rangle$ indicate an ensemble, time, or space average in order to minimize the error, enabling the dynamic model to be more stable. The ensemble averaging that was limited to homogeneous flow directions can be extended to inhomogeneous flows by using the dynamic localization procedure of Ghosal *et al.* [18] as well as the Lagrangian formulation of Meneveau, Lund, and Cabot [19]. In addition to the dynamic estimation of the Smagorinsky coefficient, the model predicts the correct behavior of the subfilter-scale viscosity in the vicinity of no-slip walls. The Smagorinsky model, on the contrary, requires a damping function in order to ensure the accurate near-wall behavior.

Nicoud and Ducros [20] proposed a model that exhibits the expected asymptotic behavior in the near-wall region, where the subfilter-scale viscosity is proportional to the cube of the wall normal distance [21]. The subfilter-scale viscosity is defined as

$$\nu_{sfs} = (C_w \Delta_{\boldsymbol{x}})^2 \frac{\left(S^d_{ij} S^d_{ij}\right)^{3/2}}{\left(\overline{S}_{ij}\overline{S}_{ij}\right)^{5/2} + \left(S^d_{ij} S^d_{ij}\right)^{5/4}}. \tag{17}$$

The coefficient C_w takes values between 0.55 and 0.6; where

$$S^d_{ij} = \overline{S}_{ik}\overline{S}_{kj} + \overline{\Omega}_{ik}\overline{\Omega}_{kj} - \tfrac{1}{3}(\overline{S}_{mn}\overline{S}_{mn} - \overline{\Omega}_{mn}\overline{\Omega}_{mn})\delta_{ij}, \tag{18}$$

with

$$\overline{\Omega}_{ij} = \frac{1}{2}\left(\frac{\partial \overline{u}_i}{\partial x_j} - \frac{\partial \overline{u}_j}{\partial x_i}\right). \tag{19}$$

There are numerous modeling attempts to accurately estimate the Smagorinsky constant. Horiuti [22] proposed a velocity scale based model, where the velocity scale was determined based on higher-order terms of anisotropic Reynolds stresses. Vreman [23] developed an algebraic framework to better predict the subfilter-scale viscosity based on fundamental realizability inequality for the theoretical subfilter-scale dissipation, which was further improved by Park *et al.* [24] by considering a global equilibrium between the subfilter-scale dissipation and the viscous dissipation. Recently, Piomelli, Rouhi, and Geurts [25] proposed and improved [26] a grid-independent definition of the subfilter-scale viscosity, and based on an integral length scale, which is computed by using turbulent kinetic energy and its dissipation.

In general, most of the subfilter-scale viscosity models are purely dissipative, i.e., they only represent the forward cascade of energy. Furthermore, they lead to a perfect alignment between the subfilter-scale stress tensor and the resolved rate-of-strain tensor, which is unphysical [15,27]. The desired properties of a subfilter-scale model are discussed by Silvis, Remmerswaal, and Verstappen [28]. The dynamic procedures [16,18,29] to compute the Smagorinsky constant results in negative subfilter-scale viscosity, a feature considered to represent the backscatter of energy. From a theoretical point of view, however, the negative dissipation may not be appropriate to represent the energy backscatter [10]. To better account for the backscatter of energy, in general, a stochastic term is often considered. For instance, Carati, Ghosal, and Moin [30] modeled the backscatter of energy in terms of negative subfilter-scale viscosity as well as a stochastic forcing term. However, as observed by Schumann [31], the stochastic forcing cannot completely describe the nonlinear interaction between the smallest resolved and largest subfilter scales, which are highly correlated.

The scale similarity models are based on the physical hypothesis that statistical flow structures are similar at different levels of the scales of motion. Liu, Meneveau, and Katz [32] successfully verified this hypothesis by using their experiments on jet turbulence and further confirmed that it persists during rapid straining. The scale similarity the model of Bardina, Ferziger, and Reynolds [33] assumes that the small resolved scales behave similar to the subfilter scales, and the subfilter-scale stress tensor constructed from resolved scales must be similar to the actual subfilter-scale stress tensor. It is expressed in terms of two cutoff levels as proposed by Liu, Meneveau, and

Katz [32]:

$$\tau_{ij} = C_b(\widetilde{\overline{u}_i\overline{u}_j} - \widetilde{\overline{u}}_i\widetilde{\overline{u}}_j). \tag{20}$$

The proportionality coefficient C_b is computed dynamically as proposed by Vreman, Geurts, and Kuerten [34]. The similarity models include the effect of backward cascade of energy and leads to good correlation with the subfilter-scale stress tensor even in anisotropic flows; however, they underestimate the dissipation. The forward energy cascade in the similarity model is improved by adding a subfilter-scale viscosity term, leading to mixed models. Bardina [35] proposed the first mixed model using a linear combination of the similarity model by using the Smagorinsky model as

$$\tau_{ij} - \tfrac{1}{3}\tau_{kk}\delta_{ij} = \tfrac{1}{2}\big(\mathcal{L}_{ij} - \tfrac{1}{3}\mathcal{L}_{kk}\delta_{ij} - 2\nu_{sfs}\overline{S}_{ij}\big). \tag{21}$$

The scale similarity model of Bardina [35] defines the total subfilter-scale stress tensor in terms of Leonard subfilter-scale stress tensor [Eq. (8)] by using a single filter cutoff, whereas Liu, Meneveau, and Katz [32] used two levels of filtering. Nevertheless, the scale-similarity models lead to much lower dissipation. The mixed models [36–38] use a subfilter-scale viscosity term to counteract the lower dissipation of the scale similarity models. In an interesting development on the scale similarity approach, Anderson and Domaradzki [39] separated the scales of turbulence in Fourier space in order to accurately model the global and interscale energy transfer and associated dissipation. The model [39] builds on prior investigations of the interscale energy transfer [40,41], where geometrical relations for the triad interactions were used to define the energy exchange among different wave-number regions, representing the small-, large-, and mixed-scale dynamics [42]. The dissipation was improved by suppressing the energy producing terms in the scales (wave-number region) near the LES filter cutoff, while preserving the characteristics of scale-similarity models. The governing equations for the large scales were directly solved, whereas the small scales were separately solved by using the subfilter-scale viscosity formulation of Smagorinsky. The approach was improved by adapting to the dynamic models [43,44] and direct analytical modeling [45].

The cross and Reynolds subfilter-scale stress tensors [Eqs. (9) and (10), respectively] involve subfilter turbulence scales, which are inaccessible in an LES; while the Leonard subfilter-scale stress tensor can be directly computed by using the resolved scales [Eq. (8)]. To incorporate effects of the interscale energy transfer (both the forward and backward), specifically between the resolved and subfilter scales, the cross and Reynolds subfilter-scale stress tensors must be accurately modeled. Zhou [46] analyzed the physical nature of the cross and the Reynolds subfilter-scale stress tensors. The cross subfilter-scale stress tensor is responsible mainly for the backscatter of subfilter-scale energy, alongside a partial contribution to the dissipation of energy; on the contrary, the Reynolds subfilter-scale stress tensor constitutes primarily the dissipation of energy, while it may contribute partially to the backward transfer of energy [46]. The majority of the subfilter-scale LES models, including the scale-similarity–based models, fall short to incorporate these mathematical and physical aspects of the cross and Reynolds subfilter-scale stresses.

In the present article, we first decompose the turbulent flow into linearly uncorrelated scales of turbulence by performing proper orthogonal decomposition (POD). Second, we express the subfilter-scale stress tensors (Leonard, cross, and Reynolds) directly in terms of the POD modes. Lastly, the scale similarity among the high-rank (low-energy) POD modes is assumed, leading to an accurate representation of the cross and Reynolds subfilter-scale stress tensors. The article is arranged as follows: Section II presents the mathematical formulation of the POD-assisted subfilter-scale model. The numerical methods are described in Sec. III, while the results are discussed in Sec. IV by using two canonical test cases: the turbulent channel flow and decaying isotropic turbulence. Furthermore, two Appendixes are included in order to demonstrate the convergence of the results (in Appendix A) and the implementation of the POD algorithm (in Appendix B).

II. PROPER-ORTHOGONAL-DECOMPOSITION–ASSISTED SUBFILTER-SCALE MODEL

Proper orthogonal decomposition (POD) is based on the two-point velocity correlation and identifies coherent flow structures containing most energy. Lumley [47] introduced POD to fluid dynamics for statistical analysis of turbulent flows. For a turbulent velocity field, POD provides an expansion in terms of orthogonal real basis functions, also called as POD modes. A key property of the POD expansion is that, for a given number of modes, it is an optimal of all decompositions of energy measures in terms of quadratic error minimization [48,49]. An instantaneous velocity $u_i(\boldsymbol{x}, t)$ in terms of POD expansion can be expressed as

$$u_i(\boldsymbol{x}, t) = \sum_{n=1}^{\infty} \phi_n^i(\boldsymbol{x}) \psi_n^i(t); \tag{22}$$

where $\phi_n^i(\boldsymbol{x})$ are the orthonormal POD modes that are invariant in time, whereas $\psi_n^i(t)$ are the space-invariant POD coefficients or modes. The bi-orthogonality of the POD expansion is explored by Aubry [50]. The POD space modes are eigenfunctions of the (Fredholm) integral equation [49]

$$\int_{-\infty}^{\infty} \langle u_i(\boldsymbol{x}, t) u_i(\boldsymbol{r}, t) \rangle \phi_n^i(\boldsymbol{x}) d\boldsymbol{r} = \lambda_n^i \phi_n^i(\boldsymbol{x}), \tag{23}$$

where λ_n^i are the corresponding eigenvalues or the modal energies. Let the POD modes be ordered in decreasing magnitude of λ_n^i such that $\lambda_1^i \geqslant \lambda_2^i \geqslant \cdots \geqslant \lambda_n^i > 0$. Then the low-rank modes, containing large energy, correspond to the large scales of flow motion; whereas the higher rank low-energy modes represent small scales of turbulence. The POD and its variants have been extensively used for identification of the coherent structures in turbulent flows [47,51,52], flow intermittency events [53], and in the development of reduced-order modeling [54–58].

Poje and Lumley [59] investigated the energy exchange mechanism between different scales of motion, providing an efficient method to extract coherent flow structures similar to the POD modes. The POD basis functions are in some sense "characteristic scales of motion" of the flow [51], and very few POD basis functions constitute most of the turbulent kinetic energy. However, the high-rank low-energy modes play a key role in accurate description of the flow, which is equivalent to the LES approach [10,60]. This is in the sense that, first, the large eddies of the flow contain most of the energy and may not be dissipative, much like the lower POD modes of a POD-Galerkin system of ordinary differential equations. Second, the smaller eddies must be accounted for their (mainly) dissipative effect; similarly, the higher POD modes, which also have dissipative effect [61], are important for the stability of a POD-Galerkin system of equations. Furthermore, the LES and POD-Galerkin system of equations require, in general, some modeling for the stability of filtered or truncated system. The filtering operation of Eq. (1) on the velocity can be expressed in terms of the POD as

$$u_i(\boldsymbol{x}, t) = \overline{u_i}(\boldsymbol{x}, t) + u_i''(\boldsymbol{x}, t) \tag{24}$$

$$= \sum_{n=1}^{N_c^i} \overline{\phi_n^i}(\boldsymbol{x}) \overline{\psi_n^i}(t) + \sum_{n=N_c^i+1}^{\infty} \overline{\phi_n^i}(\boldsymbol{x}) \overline{\psi_n^i}(t), \tag{25}$$

where N_c^i stands for the highest POD modes representing the resolved scales of motion. For decreasing size of the filter cutoff length, i.e., $\Delta_{\boldsymbol{x}} \to 0$, $N_c^i \to \infty$, whereas the subfilter contribution $u_i''(\boldsymbol{x}, t) \to 0$ and the resolved part $\overline{u}_i(\boldsymbol{x}, t) \to u_i(\boldsymbol{x}, t)$. Although the modes $\psi_n^i(t)$ are space invariant, the space filtering implicitly induces a time filtering due to the dynamics of the Navier-Stokes equations; it is conversely true for the time filtering, which induces an implicit space filtering [10].

The Leonard subfilter-scale stress tensor $\mathcal{L}_{ij}$ of Eq. (8), the cross subfilter-scale stress tensor $\mathcal{C}_{ij}$ of Eq. (9) and the Reynolds subfilter-scale stress tensor of Eq. (10) can be expressed in terms of the

POD expansion of the resolved and subfilter-scale velocities from Eqs. (24) and (25), in symbolic form, as

$$\mathcal{L}_{ij} = \sum_{n=1}^{N_c^i} \sum_{m=1}^{N_c^j} \left(\overline{\overline{\phi_n^i}\,\overline{\phi_m^j}} - \overline{\overline{\phi_n^i}}\,\overline{\overline{\phi_m^j}}\right) \overline{\psi_n^i}\,\overline{\psi_m^j}, \tag{26}$$

$$\mathcal{C}_{ij} = \left(\sum_{n=1}^{N_c^i} \sum_{m=N_c^j+1}^{\infty} + \sum_{n=N_c^i+1}^{\infty} \sum_{m=1}^{N_c^j} \right) \left(\overline{\overline{\phi_n^i}\,\overline{\phi_m^j}} - \overline{\overline{\phi_n^i}}\,\overline{\overline{\phi_m^j}}\right) \overline{\psi_n^i}\,\overline{\psi_m^j}, \tag{27}$$

$$\mathcal{R}_{ij} = \sum_{n=N_c^i+1}^{\infty} \sum_{m=N_c^j+1}^{\infty} \left(\overline{\overline{\phi_n^i}\,\overline{\phi_m^j}} - \overline{\overline{\phi_n^i}}\,\overline{\overline{\phi_m^j}}\right) \overline{\psi_n^i}\,\overline{\psi_m^j}. \tag{28}$$

The Leonard subfilter-scale stress tensor of Eq. (26) can be estimated directly by using resolved POD modes; however, the cross subfilter-scale stress tensor [Eq. (27)] must be modeled partially for the contribution of the POD modes with characteristic length scales smaller than the filter cutoff, whereas the Reynolds subfilter-scale stress tensor [Eq. (28)] requires complete modeling. The contribution of higher POD modes in the cross and Reynolds subfilter-scale stresses can be represented in terms of the highest resolved POD modes, $\overline{\phi_{N_c^i}^i}(\boldsymbol{x}, t)$.

Anderson and Domaradzki [39] considered separation of turbulence scales in Fourier space, dividing the flow energy spectrum in three discrete wave-number regions: smallest, intermediate, and largest. The nonlinear convection terms of Navier-Stokes equations were conveniently expressed in terms of the wave-number regions, categorizing their roles in the interscale energy transfer. The largest wave-number region was assumed to be the unresolved range of scales due to a spectral filtering operation, while retaining only the terms that comprised resolved wave-number regions (smallest and intermediate). Furthermore, based on the scale similarity assumption, the energy production in the intermediate wave-number region was removed to balance the effect of subfilter-scale turbulence. For the homogeneous flow directions, where the POD modes coincide with the Fourier modes [61], the two scale separation approaches (POD and Fourier decomposition) share some similarity, in addition to the assumption of the scale similarity of turbulence for the subfilter-scale turbulence modeling. There are several aspects (which are not elaborated here for brevity), however, where the two approaches differ; for instance, the binning of scales, model symmetry, and modeling of the energy exchange between the resolved and subfilter scales.

The total kinetic energy associated with the subfilter-scale POD modes is

$$K_{sfs} = \frac{1}{2} \sum_i \left(\sum_{n=N_c^i+1}^{\infty} \lambda_n^i \right). \tag{29}$$

In general, turbulent systems have high regularity, i.e., an instantaneous wave-number spectrum decays rapidly [62]. The tail of the wave-number spectrum in turbulence decays exponentially (see Tennekes and Lumley [63]). Berkooz, Holmes, and Lumley [48] established a connection between the tail of the wave-number spectrum and tail of the eigenvalues of POD, and showed that the tail of the POD eigen-spectrum decays faster than any other basis due to the maximization of energy principle of the POD. However, the regularity results are relevant to the far dissipative range of turbulence or the very high order of POD modes [64]. Couplet, Sagaut, and Basdevant [60] describe the global features of energy transfers between the POD modes in a turbulent flow. The transfer of energy between the POD modes is local, similar to the local exchange of energy between the Fourier modes [65,66]. Furthermore, Couplet, Sagaut, and Basdevant [60] confirm the local forward and backward transfer of energy in time and space, in addition to the overall forward transfer of energy, in the mean sense, from the low-rank to high-rank POD modes. The effective forward transfer (drain) of the modal energy can be obtained in terms of the POD eigenvalues. Assuming the scale similarity between the highest resolved and subfilter-scale POD modes, the drain of the modal

energy at the filter cutoff can be expressed in terms of a ratio, β_i, as

$$\beta_i = \frac{\lambda^i_{N^i_c}}{\lambda^i_{N^i_c-1}}, \tag{30}$$

which is further assumed to be constant for the subfilter-scale (higher rank) POD modes. The energy contribution of the higher POD modes, $n > N_c$, can be approximated in terms of the coefficients, α_i, defined as

$$\alpha_i = \left(1 + \sum_{n=N^i_c+1}^{\infty} \beta_i^{(n-N^i_c)}\right)^{1/2}. \tag{31}$$

The amount of modal energy associated with a mode of rank n with respect to its lower rank mode $n-1$ is assumed to be constant for all the subfilter-scale modes, in terms of a constant value of the parameter β_i. The cross and Reynolds subfilter-scale stresses can be approximated as

$$\mathcal{C}_{ij} \approx \alpha_j \sum_{n=1}^{N^i_c} \left(\overline{\overline{\phi^i_n \phi^j_{N^j_c}}} - \overline{\overline{\phi^i_n}}\,\overline{\overline{\phi^j_{N^j_c}}}\right)\overline{\psi^i_n}\,\overline{\psi^j_{N^j_c}} + \alpha_i \sum_{m=1}^{N^j_c} \left(\overline{\overline{\phi^i_{N^i_c}\phi^j_m}} - \overline{\overline{\phi^i_{N^i_c}}}\,\overline{\overline{\phi^j_m}}\right)\overline{\psi^i_{N^i_c}}\,\overline{\psi^j_m}, \tag{32}$$

$$\mathcal{R}_{ij} \approx \alpha_i \alpha_j \left(\overline{\overline{\phi^i_{N^i_c}\phi^j_{N^j_c}}} - \overline{\overline{\phi^i_{N^i_c}}}\,\overline{\overline{\phi^j_{N^j_c}}}\right)\overline{\psi^i_{N^i_c}}\,\overline{\psi^j_{N^j_c}}. \tag{33}$$

The ensemble averaging used in Eq. (23) can be substituted with a time averaging under the assumption of the ergodicity of flow [61]. Regardless of the ergodicity of flow, the time averaging can be used to obtain the POD modes provided that it converges and satisfies the conditions of the Hilbert-Schimidt and Mercer theorems [61]. There are two difficulties while solving Eq. (23): first, performing such an averaging during a LES is not possible due to the inaccessibility of the future time solutions and, second, the number of degrees of freedom of the space correlation matrix can be very high, which equals the square of the number of computational grid points. To remedy this, the POD modes can be obtained by the snapshot method proposed by Sirovich [67], where a set of time solutions is used to compute a temporal correlation and an analogous integral equation is solved for the eigenvalue problem. Traditionally, POD has been employed for eduction of the large coherent flow structures and modes that represent the global statistics of a system, thus the ensemble averaging over homogeneous directions of flow as well as the long-time statistical averaging are regularly implemented. However, in the context of subfilter-scale dynamics, our interest lies in the highest resolved POD modes and short-time evolving dynamics. Thus a short-time snapshot POD is anticipated to provide the transient energy contribution of the subfilter-scale modes via Eqs. (30) and (31), by substantially reducing the cost of POD.

The subfilter-scale stresses [Eqs. (26), (32), and (33)] require application of the filtering operation twice. As anticipated by Germano [68], a multiple level short-time filtering should lead to a local statistics of the turbulence, analogous to the wavelet analysis that provides a local spectral picture of the flow. To complement the requirement of the snapshot POD, namely, caching a set of time solutions, a continuous causal filter of the form [69]

$$\widetilde{\varphi}(\boldsymbol{x}, t) = \int_{-\infty}^{t} \varphi(\boldsymbol{x}, t - t') G(t', \Delta_t) dt', \tag{34}$$

can be conveniently used. The characteristic cutoff time, Δ_t, is equivalent to the space filter cutoff $\Delta_{\boldsymbol{x}}$. Furthermore, it is uniform in the space and can be estimated based on a turnover time of the highest resolved POD mode, $\overline{\psi^i_{N^i_c}}(t)$. The kernel

$$G(t, \Delta_t) = \frac{1}{\Delta_t} H(t + \Delta_t), \tag{35}$$

where $H(t)$ is the Heaviside function, leads to

$$\widetilde{\varphi}(\boldsymbol{x},t)=\frac{1}{\Delta_t}\int_{t-\Delta_t}^{t}\varphi(\boldsymbol{x},t')dt'. \tag{36}$$

The temporal filtering, in general for Navier-Stokes equations, results in frame-invariant velocity under the Galilean group of transformations [69]; in the context of LES, it is also true for the subfilter-scale velocity [70]. However, the subfilter-scale velocity is not frame-invariant under the Euclidean group of transformations [70]; unlike for the spatially filtered LES [5]. Applying the causal filter and rearranging [Eqs. (26), (32), and (33)] leads to the subfilter-scale stress tensor of Eq. (7):

$$\begin{aligned}\tau_{ij}\approx&\underbrace{\sum_{n=1}^{N_c^i}\sum_{m=1}^{N_c^j}\big(\widetilde{\overline{\psi_n^i}\,\overline{\psi_m^j}}-\widetilde{\overline{\psi_n^i}}\,\widetilde{\overline{\psi_m^j}}\big)\overline{\phi_n^i}\,\overline{\phi_m^j}}_{\mathcal{L}_{ij}}\\&+\underbrace{\alpha_j\sum_{n=1}^{N_c^i}\big(\widetilde{\overline{\psi_n^i}\,\overline{\psi_{N_c^j}^j}}-\widetilde{\overline{\psi_n^i}}\,\widetilde{\overline{\psi_{N_c^j}^j}}\big)\overline{\phi_n^i}\,\overline{\phi_{N_c^j}^j}+\alpha_i\sum_{m=1}^{N_c^j}\big(\widetilde{\overline{\psi_{N_c^i}^i}\,\overline{\psi_m^j}}-\widetilde{\overline{\psi_{N_c^i}^i}}\,\widetilde{\overline{\psi_m^j}}\big)\overline{\phi_{N_c^i}^i}\,\overline{\phi_m^j}}_{\mathcal{C}_{ij}}\\&+\underbrace{\alpha_i\alpha_j\big(\widetilde{\overline{\psi_{N_c^i}^i}\,\overline{\psi_{N_c^j}^j}}-\widetilde{\overline{\psi_{N_c^i}^i}}\,\widetilde{\overline{\psi_{N_c^j}^j}}\big)\overline{\phi_{N_c^i}^i}\,\overline{\phi_{N_c^j}^j}}_{\mathcal{R}_{ij}}.\end{aligned} \tag{37}$$

The exact expressions of the Leonard [Eq. (26)], cross [Eq. (27)], and Reynolds [Eq. (28)] subfilter-scale stresses in terms of the POD modes preserve the realizability of the total subfilter-scale stress tensor (τ_{ij}). Similar to the statistically averaged Reynolds stress tensor, which is also a positive-semidefinite (or realizable) tensor [71], the subfilter-scale tress tensor must satisfy the following inequalities for the realizability [6]:

$$\tau_{ii}\geqslant 0, \tag{38}$$

$$\tau_{ij}^2\leqslant\tau_{ii}\tau_{jj}, \tag{39}$$

$$\det\left(\tau_{ij}\right)\geqslant 0. \tag{40}$$

The ratio of eigenvalues β_i [Eq. (30)] is always in $0<\beta_i\leqslant 1$, consequently, the coefficients α_i [Eq. (31)] are always >1, which retains the non-negativity of the trace of subfilter-scale stress tensor. Thus, the modeling of subfilter-scale stress [Eq. (37)] in terms of the highest resolved POD modes and the model parameters β_i and α_i still guarantees the first inequality [Eq. (38)]. However, it is a necessary but not sufficient condition for the realizability.

III. NUMERICAL METHOD

The governing flow equations (4) and (5), are solved by using a collocated finite-volume solver [72,73] (see code-saturne.org). A second-order central time marching of the incompressible Navier-Stokes equations is achieved by using the Crank-Nicolson scheme [74], which is similar to the SIMPLEC algorithm [75]. The time step is constant in time and uniform in space. A fractional step scheme is used to solve the mass and momentum equation (refer to Chorin [76]), which includes a prediction step for the velocity components with an explicit pressure gradient, a pressure correction step by solving the Poisson equation with a conjugate gradient method, and enforcing the mass conservation. The interpolation of Rhie and Chow [77] is used when solving the pressure to avoid oscillations, which introduces some numerical dissipation, removing energy equally at all wave

numbers. This interpolation [77] has a stabilizing effect for nonuniform grids, preventing the odd-even decoupling phenomenon in the solver that is otherwise kinetic-energy conserving [78]. The subiterations on the predictor-corrector algorithm for the pressure or velocity coupling alongside the Rhie and Chow [77] interpolation improve the convergence and, to some degree, the kinetic-energy conservation. The convection-diffusion terms are spatially discretized by using a second-order centered scheme. The linear system for the velocity is solved by means of Gauss-Seidel, whereas the gradient reconstruction is performed by using a robust iterative process, achieving the solver precision of 10^{-8} in all simulations.

Numerical discretization of the Navier-Stokes equations introduces spatial and temporal scales associated with the computational grid and time stepping, which are supposed to be much smaller compared with the cutoff length scale of an LES filter [see, e.g., Eq. (1)] to ensure a smaller discretization error. The decoupling of the filter cutoff length from the discretization scales, also called prefiltering [79], require explicit filtering [80–83], which is computationally expensive. Therefore it is practical to consider the filter cutoff length equivalent to the grid size. The top-hat filter [Eq. (3)] is compatible with the finite-volume discretization [84]. To reduce the computational cost, it is useful to define filters with varying cutoff length, for example, near the no-slip walls or in the region of solution with steep gradients. However, it is inconsistent with the homogeneity and isotropy assumptions, which leads to nonzero commutation errors for the filtering and differentiation operations. A general definition in terms of change of variable enables the use of homogeneous filters, which commute at the second order with the differentiation [10,85]. The properties of the top-hat filter for inhomogeneous cases, where the filter cutoff length varies in space, are described by Ghosal and Moin [85].

As discussed in Sec. I, the dynamic Smagorinsky model uses an explicit second filter or a test filter with a larger cutoff length. In the present flow solver, the default size of the test filter is twice that of the computational grid size. The averaging of the numerator and denominator in Eq. (15), in a general case, is performed locally over the extended neighboring grids (grids that share at least one vertex with the considered grid cell). The trace of the subfilter-scale stress tensor, $\frac{1}{3}\tau_{kk}$, is added to the pressure term. The dynamic computation of the Smagorinsky constant may lead to negative values of the total viscosity ($\nu + \nu_{sfs}$), which is avoided by clipping the negative values to zero.

The subfilter-scale stress term, $-\frac{\partial \tau_{ij}}{\partial x_j}$, of Eq. (5) must be solved directly in the proposed POD-assisted formulation. To be consistent with the convection-diffusion terms and preserve the time convergence, the subfilter-scale stress term is also discretized by using the second-order scheme. The cutoff size Δ_t of the causal temporal filter in Eq. (36) is estimated by using the temporal modes, $\overline{\psi^i_{N^i_c}}(t)$. A simple time-correlation provides the three values of the turnover time corresponding to the three velocity components, and the minimum value is selected as the cutoff Δ_t. The flow solutions are collected over this time (Δ_t) to perform the short-time snapshot POD. Thus, the number of snapshots approximates the ratio of the cutoff time to the simulation time step. Most importantly, the resolved POD modes satisfy

$$\lambda^i_n = \left\langle \overline{\psi^i_n}^2 \right\rangle_{\Delta_t}, \tag{41}$$

which leads to the cutoff POD mode number, N^i_c. The short-time snapshot-POD procedure is discussed in more detail in Appendix B.

IV. RESULTS AND DISCUSSION

In this section, we present the results of simulations performed using the proper orthogonal decomposition assisted subfilter-scale model for two canonical cases: turbulent channel flow and decaying isotropic turbulence. The results for the turbulent channel flow are discussed in comparison with the direct numerical simulations (DNS) as well as the dynamic Smagorinsky (DSM) and wall-adapting local eddy-viscosity (WALE) models. The classical experiment of Comte-Bellot and

TABLE I. Simulation details.

Model	Re_b	u_τ	Δx^+	Δy_w^+	Δy_c^+	Δz^+
DNS	10000	0.054450	8.90	≈0.0027	4.53	5.01
DSM	9839	0.054469	35.64	0.5447	8.357	13.37
WALE	9961	0.054119	35.42	0.5412	8.304	13.28
PODA	9508	0.054429	35.62	0.5443	8.351	13.36

Corrsin [86] on isotropic decaying turbulence is also simulated by using the three LES models in Sec. IV B.

A. Turbulent channel flow

Turbulent channel flow at Reynolds number $Re_b \approx 10\,000$ ($Re_\tau \approx 544$) is simulated by using the presented POD-assisted (PODA) model. Re_b and Re_τ are the Reynolds numbers based on the bulk velocity u_b and friction velocity u_τ, respectively, as well as the channel height h. The bulk and friction velocities are defined as

$$u_b \equiv \frac{1}{h}\int_0^h \langle u_x \rangle dy \quad \text{and } u_\tau \equiv \sqrt{\tau_w/\rho}, \tag{42}$$

respectively, where τ_w is the wall shear stress. The channel dimensions are $4\pi h$, $2h$, $3\pi h/2$ in the streamwise X, wall normal Y, and spanwise Z directions, respectively. The boundaries normal to the Y direction are assigned with a no-slip wall condition, while the flow is periodic in the other two, streamwise X and spanwise Z, directions. The mean flow is in the $+X$ direction, which is maintained by a body force in terms of the mean pressure gradient as [1]

$$-\frac{dp}{dx} = \frac{\rho u_\tau^2}{h}. \tag{43}$$

The computational domain is discretized by using 192, 308, and 192 finite volumes in the X, Y, and Z directions, respectively. The mesh is uniform in the X and Z directions. In the Y direction, the first mesh point is placed such that the nondimensional wall distance, $y^+ = yu_\tau/\nu$, remains less than unity; while the mesh is stretched away from the no-slip wall by using geometric progression with a growth ratio of 1.02.

The flow configuration of the channel is adopted from the DNS database of Lee and Moser [87] for the same Reynolds number. The first row of Table I provides more details of the DNS, where Δx^+ and Δz^+ are the nondimensional mesh resolutions in the X and Z directions, respectively. The wall unit quantities, throughout the article, that are indicated by superscript "+" are normalized by using the friction velocity u_τ and kinematic viscosity ν. In the DNS, the distance of the first computational point away from the no-slip wall (in wall units) is $\Delta y_1^+ \approx 0.000\,27$, whereas the mesh resolution at the center of the channel in the Y direction is $\Delta y_c^+ = 4.53$. The kinematic viscosity ν and friction velocity u_τ in the DNS are 1×10^{-4} m^2/s and $u_\tau = 5.434\,96 \times 10^{-2}$ m/s, respectively.

The simulations are performed by using the three LES models (DSM, WALE, and PODA) for approximately 240 flow passes through the channel, after the initial transient, ensuring a converged statistics. Further details on the results convergence are provided in Appendix A. The statistics are gathered along the wall normal direction, between $y = 0$ and $y = h$, at the midpoint of the channel ($x = 2\pi h$, $z = 3\pi h/4$). Rows 2, 3, and 4 of Table I provide details of the simulations performed by using the DSM, WALE, and PODA models, respectively, in terms of the bulk Reynolds number, friction velocity, and mesh resolutions in the wall units. Although the simulations for the three LES models (DSM, WALE, and PODA) are performed on the same mesh, the mesh resolution in wall units differ (Table I) to some degree due to the difference in friction velocity u_τ predictions, which are within ≈0.03% of the relative error compared with the friction velocity for the DNS.

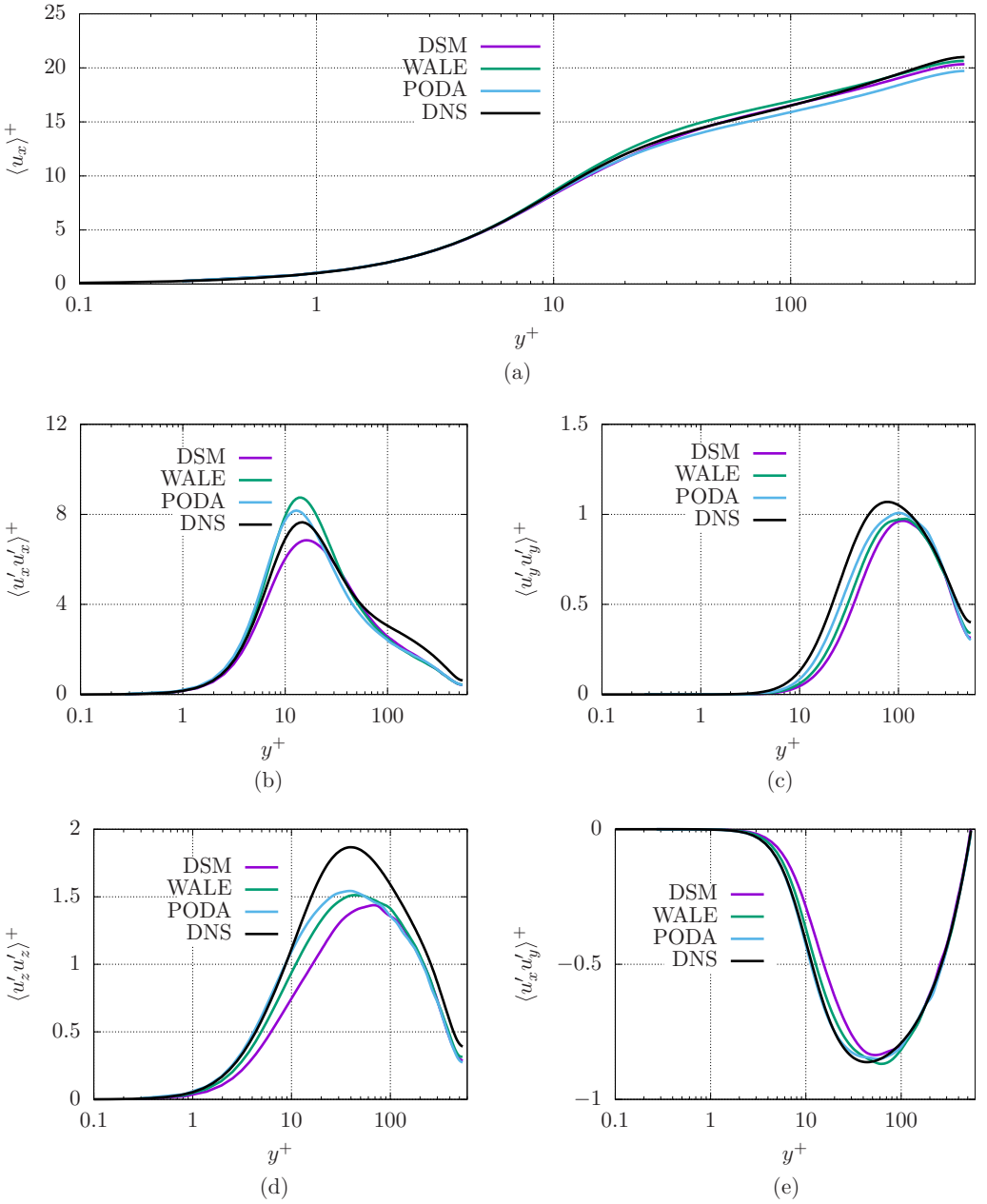

FIG. 1. Comparison of time-averaged streamwise velocity and Reynolds stresses. (a) Time-averaged streamwise velocity. (b) Reynolds stress component comprising the x velocity fluctuations. (c) Reynolds stress component comprising the y velocity fluctuations. (d) Reynolds stress component comprising the z velocity fluctuations. (e) Reynolds stress component comprising the x and y velocity fluctuations.

The time-averaged flow statistics in terms of the streamwise velocity and Reynolds stresses is presented in Fig. 1. The mean streamwise velocity $\langle u_x \rangle^+$ profiles that are predicted by the three models, Fig. 1(a), are in a reasonable agreement with the DNS results. The WALE subfilter-scale viscosity model tends to over predict the mean velocity at about $y^+ \approx 40$, whereas the PODA

TABLE II. Comparison of central processing unit (CPU) time.

DSM	WALE	PODA
1.0	0.83	1.12

model, to some degree, under predicts the mean velocity for $y^+ \gtrapprox 100$. The Reynolds stress component $\langle u'_x u'_x \rangle^+$, Fig. 1(b), is well predicted by the three models; however, the profiles show some discrepancies in the buffer region ($10 \lessapprox y^+ \lessapprox 40$) as well as the $y^+ \gtrapprox 100$ region of the boundary layer. The $\langle u'_y u'_y \rangle^+$ and $\langle u'_z u'_z \rangle^+$ components of the Reynolds stress tensor, displayed in Figs. 1(c) and 1(d), respectively, are better captured by the PODA when compared with the DSM and WALE models. Lastly, the deviatoric component $\langle u'_x u'_y \rangle^+$, Fig. 1(e), predicted by the PODA and WALE models show a good agreement with the DNS profile, while DSM slightly overpredicts the values for $10 \lessapprox y^+ \lessapprox 100$.

A comparison of the computational cost among the DSM, WALE, and PODA models is provided in Table II. The speed-ups for the WALE and PODA models with reference to the DSM are 0.83 and 1.12, respectively. The central processing unit (CPU) time for the PODA model can be reduced by lowering the disk input-output overhead of the flow solutions that is required for the on-the-fly snapshot POD.

The one-dimensional energy spectra of the streamwise velocity along the spanwise direction are shown in Fig. 2, where the spectra are normalized by u_τ^2. The longitudinal energy spectra at $y^+ = 541$ that are predicted by the three models in comparison with the DNS spectrum are shown in Fig. 2(a), while the spectral comparison at $y^+ = 18.11$ is displayed in Fig. 2(b). The energy spectra near the center of channel ($y^+ = 541$), Fig. 2(a), exhibit the $-5/3$ behavior for the wave-number range $10 \lessapprox k_z h \lessapprox 50$, indicating the inertial subrange [1]. The implicit filter (numerical grid) cutoff for the three LES models is at $k_z h = 128$, which is towards the higher end (in terms of the wave number) of the inertial subrange. The spectra predicted by the DSM and WALE model show lower energy levels when compared with the PODA spectrum, particularly near the filter cutoff ($k_z h \gtrapprox 40$). The energy spectra in the near-wall buffer region (at $y^+ = 18.11$) exhibit relatively shorter inertial subrange ($30 \lessapprox k_z h \lessapprox 50$), as shown in Fig. 2(b). The higher magnitudes of $\langle u'_x u'_x \rangle^+$ for the WALE and PODA models in the buffer region [Fig. 1(b)] are also reflected in the energy spectra of Fig. 2(b), where the WALE and PODA models exhibit higher energy for $k_z h \gtrapprox 30$ when compared with the DNS and DSM spectra.

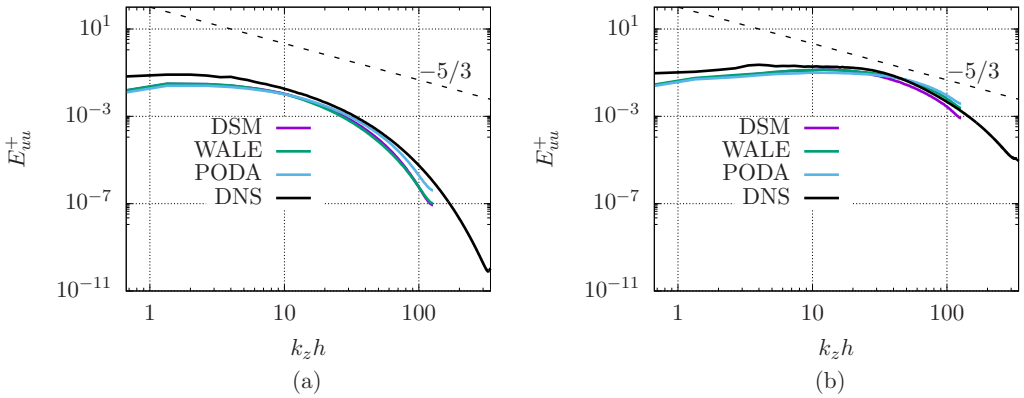

FIG. 2. Energy spectra of the streamwise velocity component along the spanwise direction (a) near the center of the channel (at $y^+ = 541$) and (b) in the buffer region (at $y^+ = 18.11$).

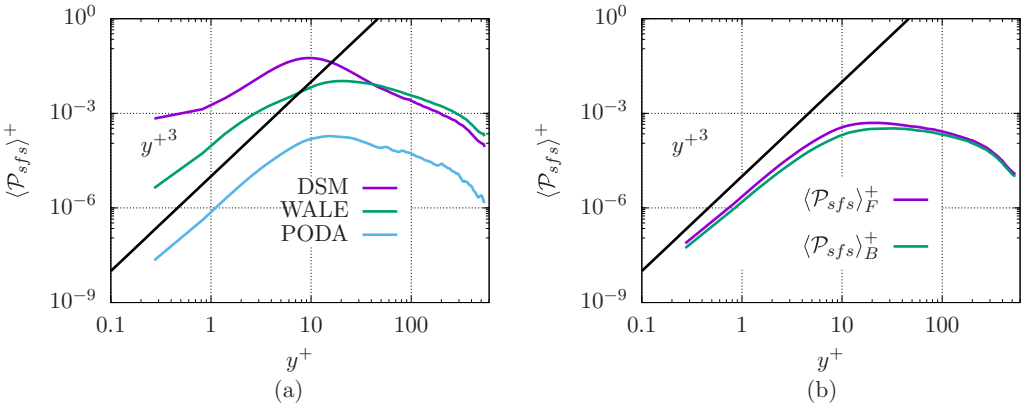

FIG. 3. Time-averaged energy transfer between the resolved and subfilter-scales. (a) Total energy transfer to subfilter-scales. (b) Forward and backward energy transfer.

The transfer of energy from the resolved scales to the subfilter-scales is given as

$$\mathcal{P}_{sfs} = -\tau_{ij}\overline{S}_{ij}, \tag{44}$$

which is also known as the production of subfilter-scale energy. For the LES filter cutoff in the inertial subrange, the time-averaged $\mathcal{P}_{sfs}$ equals the dissipation of kinetic energy, which is positive only; however, it can become negative instantaneously due to inviscid, inertial processes [1]. The time-averaged subfilter-scale production of kinetic energy for the three models is shown in Fig. 3(a), where the normalized production is obtained by $\langle \mathcal{P}_{sfs} \rangle^+ = \langle \mathcal{P}_{sfs} \rangle \nu / u_\tau^4$. In the limit $y^+ \to 0$, the resolved rate-of-strain tensor $\overline{S}_{ij}$ follows $O(1)$ [20], whereas the elements of subfilter-scale stress tensor τ_{ij} exhibits different power laws based on the velocity components, leading the subfilter-scale energy production to follow $O(y^{+3})$.

The three LES models, as shown in Fig. 3(a), exhibit the accurate near-wall behavior by following the $O(y^{+3})$ power law; however, the DSM and WALE models produce much higher subfilter-scale energy compared with the PODA model. In the log-layer region, $y^+ \gtrapprox 30$, the DSM and WALE models produce the subfilter-scale energy at approximately the same order of magnitude, whereas in the near-wall region the DSM is more dissipative compared with the WALE and PODA. The DSM and WALE models are purely dissipative, as they only account for the transfer of energy from the resolved scales to subfilter scales in terms of the subfilter-scale viscosity ν_{sfs}. As noted before, the production of subfilter-scale energy can be negative instantaneously, leading to backward transfer of energy from the subfilter-scales to the resolved scales. The DSM model predicts negative values for the Smagorinsky constant, an indication of the backward transfer of energy from the subfilter-scales; however, from a theoretical point of view the backward energy cascade is not associated with the negative subfilter-scale viscosity [10]. Furthermore, the negative values of the subfilter-scale viscosity are clipped to avoid the negative value of total viscosity $(\nu + \nu_{sfs})$ and possible numerical instability.

The PODA model exhibits a considerable amount of backward transfer of energy, an observation consistent with the theoretical work of Chasnov [9] as well as the DNS results of Piomelli *et al.* [88] and Domaradzki, Liu, and Brachet [40], which show that the backscatter and forward cascade of energy are of the same order magnitude, resulting in lower values of the time-averaged effective production of the subfilter-scale energy [Fig. 3(a)]. Figure 3(b) shows the time-averaged forward and backward transfer of energy, denoted by $\langle \mathcal{P}_{sfs} \rangle_F^+$ and $\langle \mathcal{P}_{sfs} \rangle_B^+$, respectively. The peaks of the forward and backward energy transfer occur in the buffer region at $y^+ \approx 12$, which is also the region of peak turbulent kinetic energy; similar results were obtained by Piomelli *et al.* [88] for the channel flow at a lower Reynolds number $Re_b = 3300$, where the peaks of forward and backward transfer of energy

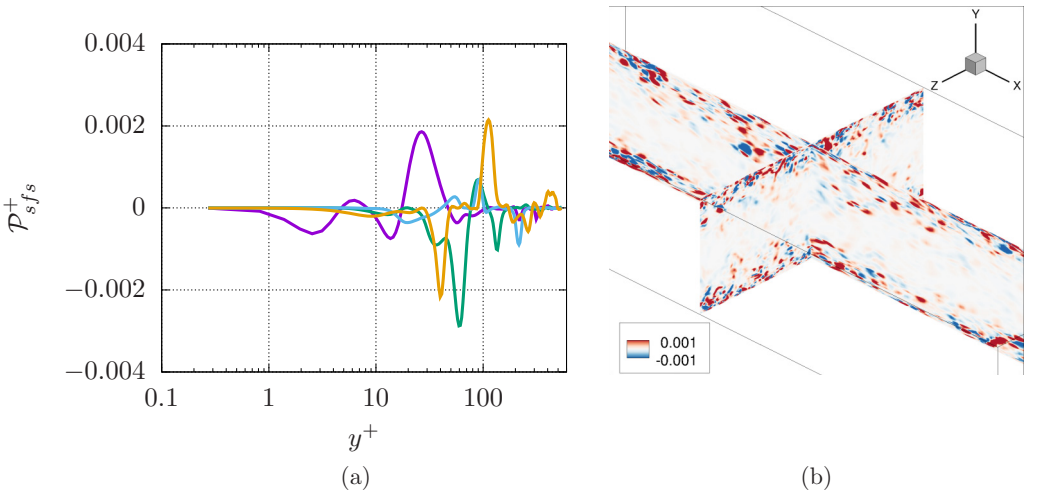

FIG. 4. Instantaneous energy transfer between the resolved and subfilter-scales. (a) Instances of subfilter-scale production, $\mathcal{P}^+_{sfs}$. (b) Instantaneous subfilter-scale production, $\mathcal{P}^+_{sfs}$.

were observed also at $y^+ \approx 12$. Here, the backscatter of energy $\langle \mathcal{P}_{sfs} \rangle^+_B$ constitutes nearly 75% of the forward transfer $\langle \mathcal{P}_{sfs} \rangle^+_F$ in the log-layer, which further increases for increasing wall distance, leading to ≈85% towards the center of the channel. In the buffer layer region the backward energy transfer is approximately 65% of the forward energy transfer, which decreases to 55% for $y^+ \approx 10$; however, this percentage increases for further decrease in the wall normal distance, which tends to ≈65% near the wall. The ratio $\langle \mathcal{P}_{sfs} \rangle^+_F / \langle \mathcal{P}_{sfs} \rangle^+_B$ behaves like $O(y^{+0.15})$ in the near-wall region (for $y^+ \lesssim 10$). Figure 4 shows the instantaneous production of the subfilter-scale energy, $\mathcal{P}^+_{sfs}$, along the wall normal distance [Fig. 4(a)] and in the vertical mid-planes [Fig. 4(b)] of channel, where the instantaneous production shows peaks of positive and negative values near the buffer layer region.

The LES subfilter-scale models that are based on the dissipation of kinetic energy from the resolved scales to subfilter-scales entail the filter cutoff to be in the inertial or dissipative range of the energy spectrum. However, it is desired to use a large filter cutoff length and incorporate only the large scales of motion in order to reduce the computational cost. The construct of the PODA model is based on the similarity among the scales near the filter cutoff, allowing the use of larger filter cutoffs. Here we consider a filter cutoff that is ≈20% larger than the small filter; the small filter cutoff corresponds to mesh M1 in Table III, whereas the larger one corresponds to mesh M2. Table III provides more details on the mesh resolution and friction velocity estimates. The values of friction velocity for the meshes M1 and M2 are 5.4429×10^{-2} and 5.4157×10^{-2}, respectively; for the nominal mesh M2, it leads to a mesh resolution of $\Delta x^+ = 42.54$, $\Delta y^+_c = 13.76$, and $\Delta z^+ = 15.95$.

The time-averaged flow statistics in terms of the streamwise velocity and Reynolds stresses for the two grids are compared with the DNS results in Fig. 5, where the model predictions for the nominal mesh M2 are reasonable. The time-mean streamwise velocity $\langle u_x \rangle^+$, Fig. 5(a), for the

TABLE III. Details of the two mesh resolutions.

Mesh	Re_b	u_τ	Δx^+	Δy^+_w	Δy^+_c	Δz^+
M1	9508	0.054429	35.62	0.5443	8.351	13.36
M2	9535	0.054157	42.54	0.5415	13.76	15.95

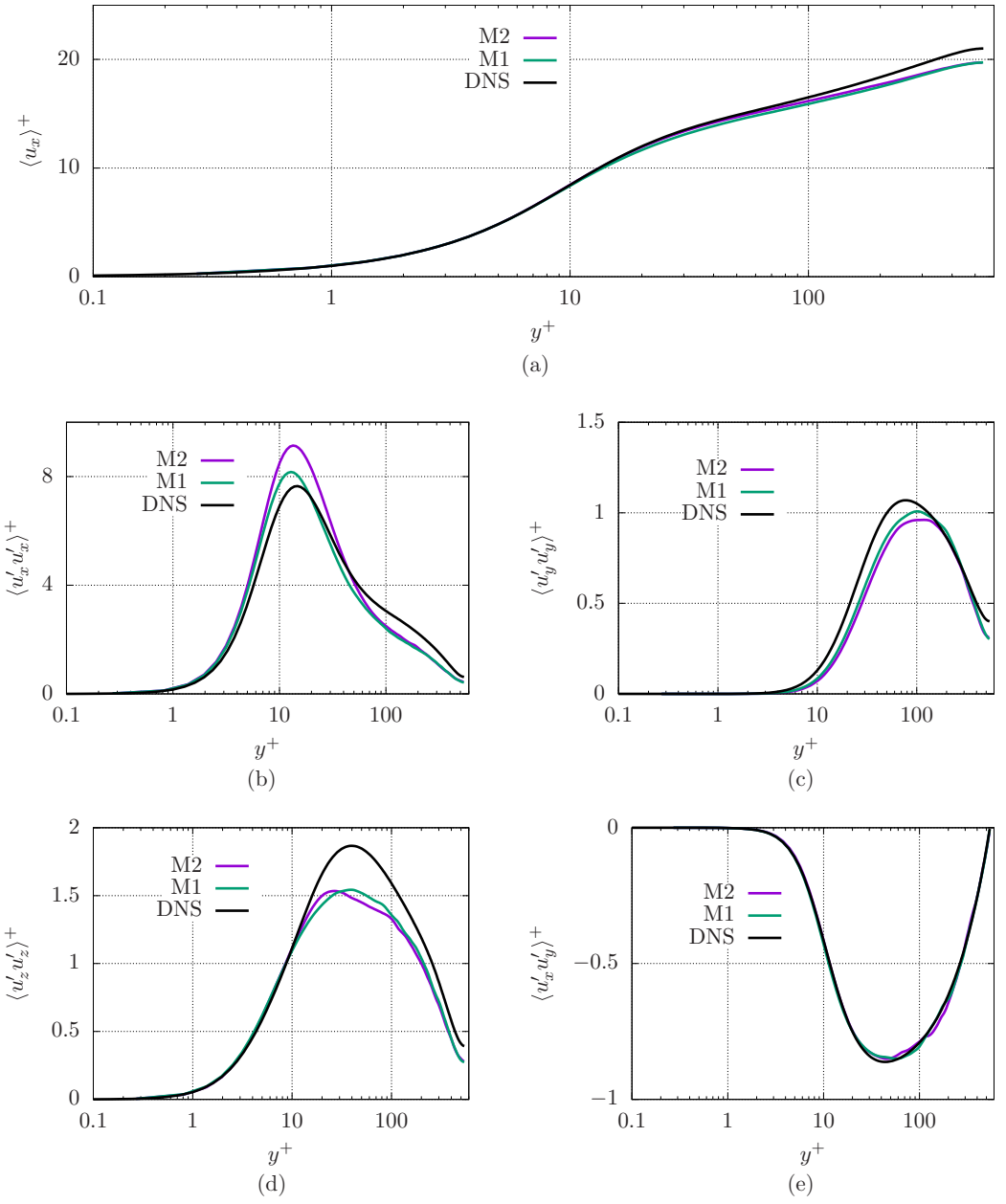

FIG. 5. Mean flow and Reynolds statistics for the two mesh resolutions. (a) Time-averaged streamwise velocity. (b) Reynolds stress component comprising the x velocity fluctuations. (c) Reynolds stress component comprising the y velocity fluctuations. (d) Reynolds stress component comprising the z velocity fluctuations. (e) Reynolds stress component comprising the x and y velocity fluctuations.

nominal mesh M2 shows a good agreement with the finer mesh M1 and DNS profiles. The diagonal components of the Reynolds stress tensor $\langle u'_i u'_i \rangle^+$, Fig. 5(b) through Fig. 5(d), for the nominal mesh M2 exhibit minor discrepancies, particularly in the buffer layer region when compared with the finer mesh M1 as well as DNS profiles. The deviatoric component $\langle u'_x u'_y \rangle^+$ of Fig. 5(e), on the other hand, manifests a good agreement between both the mesh resolutions as well as with the DNS profile.

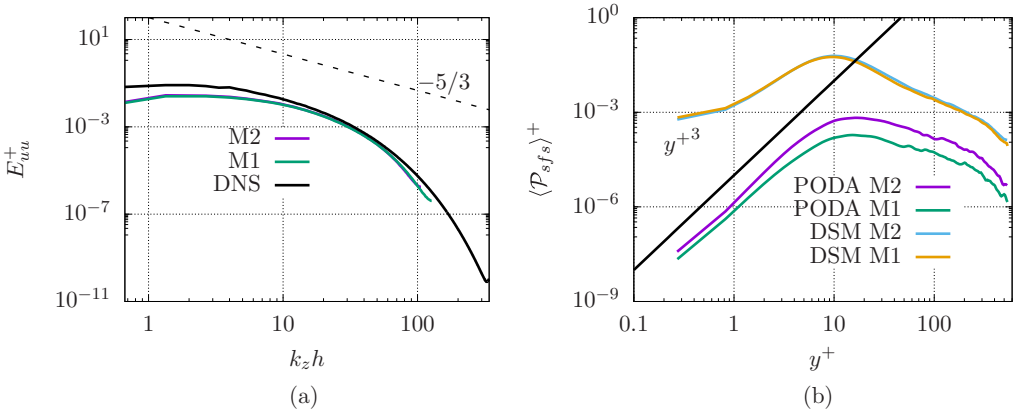

FIG. 6. Comparison of the energy spectra and subfilter-scale energy production for the two mesh resolutions. (a) Spanwise energy spectra of the streamwise velocity at $y^+ = 541$. (b) Time-averaged subfilter-scale energy production.

The energy spectra of the streamwise velocity in the spanwise direction at $y^+ = 541$ for the two mesh resolutions (Table III) are shown in Fig. 6(a). The filter cutoff for the meshes M1 and M2 correspond to the spanwise wave numbers of $k_z h = 128$ and $k_z h = 106.67$, respectively, compared with $k_z h \approx 341$ for the DNS. However, for both the mesh resolutions, the filter cutoffs lie towards the higher end (in terms of the wave number) of the inertial subrange [Fig. 6(a)]. The normalized energy spectra [Fig. 6(a)] for both the mesh resolutions show a reasonable agreement with the DNS energy spectrum, with some under-prediction of energy towards the lower and higher ends of (the LES) spectra.

The time-averaged production of subfilter-scale energy, $\langle \mathcal{P}_{sfs} \rangle^{+}$, for the two filter cutoff cases is shown in Fig. 6(b). In addition to the PODA model, the figure includes a comparison of the subfilter-scale energy production for the two mesh resolutions for the DSM. The subfilter-scale production follows the near-wall y^{+3} power law for both the mesh resolutions. As anticipated, the subfilter-scale production increases for increasing filter cutoff size, i.e., for the nominal mesh, particularly in the log-layer region ($y^+ \gtrapprox 10$). In general, a similar trend is observed for the DSM, where the nominal mesh M2 results in, to some degree, higher production of subfilter-scale energy [Fig. 6(b)].

As discussed before, the causal filter in Eq. (36) applies a temporal cutoff equivalent to the spatial filter cutoff due to the spatiotemporal properties of Navier-Stokes equations. The temporal filter cutoffs equivalent to the spatial filter cutoffs associated with the two mesh resolutions M1 and M2 are provided in Table IV. The size of the causal filter cutoff $\langle \Delta_t \rangle^{+}$, normalized by ν/u_τ^2, increases for the nominal mesh M2 compared with the finer mesh M1. The energy ratio of the

TABLE IV. Effect of mesh resolution (filter size) on the model parameters.

	M1	M2
$\langle \Delta_t \rangle^{+}$	1.0369	1.3492
$\langle \beta_x \rangle$	1.56×10^{-5}	2.19×10^{-5}
$\langle \beta_y \rangle$	2.74×10^{-3}	3.03×10^{-3}
$\langle \beta_z \rangle$	2.68×10^{-3}	3.25×10^{-3}
$\langle \alpha_x \rangle$	$1 + 1.76 \times 10^{-6}$	$1 + 1.32 \times 10^{-5}$
$\langle \alpha_y \rangle$	$1 + 1.27 \times 10^{-3}$	$1 + 1.29 \times 10^{-3}$
$\langle \alpha_z \rangle$	$1 + 1.24 \times 10^{-3}$	$1 + 1.41 \times 10^{-3}$

highest (low-energy) resolved POD modes, i.e., β_i of Eq. (30), and the modal coefficient α_i increase (Table IV) for the nominal mesh M2 when compared with the finer mesh M1.

The total subfilter-scale stress as well as the individual subfilter-scale stresses (Leonard, cross and Reynolds tensors) are functions of both the space and time, representing local and global complex interactions among the turbulence scales [1,32]. Thus the subfilter-scale model coefficients are desired to be a function of local flow variables, varying in space and time such that the model is applicable for flows involving inhomogeneous directions and/or complex geometries [18,19]. The mathematical formulation of PODA model naturally ensures the local-global and space-time properties of the subfilter-scale stress tensors, because of the scale similarity of turbulence. However, the absolute time-local nature of the PODA model is, to some extent, compromised due to the short-time snapshot POD procedure. The time locality is restricted to the turnover time of smallest eddies, corresponding to the highest resolved (low-energy) POD modes. The estimation of subfilter-scale stress tensor [Eq. (37)] comprises all resolved POD modes, incorporating the effect of global and local flow scales, which span across the entire domain as well as evolve in time. Importantly, the transfer of energy between the resolved and subfilter scales is modeled in terms of the POD modal energies λ^i, which are global in space and local (or rather pseudolocal due to the short-time snapshot POD) in time; the transfer of energy is local in space, because it follows the spatial support of the POD modes, as well as time.

The highest resolved or cutoff POD modes ($\overline{\phi^i_{N_c^i}}$, $\overline{\psi^i_{N_c^i}}$) are crucial for the modeling of the cross and Reynolds subfilter-scale stresses, as described in Sec. II. Figure 7 displays the highest resolved POD space and time modes for an arbitrary state in the LES simulation, where the orthonormal POD space modes for the streamwise ($\overline{\phi^u_{N_c^u}}$), wall normal ($\overline{\phi^v_{N_c^v}}$), and spanwise ($\overline{\phi^w_{N_c^w}}$) components of velocity are shown in Figs. 7(a)–7(c), respectively. The corresponding orthogonal POD time modes ($\overline{\psi^i_{N_c^i}}$) are shown in Fig. 7(d), where they are normalized by the square root of their corresponding eigenvalues. At this arbitrary state, the turnover time (Δ_t) and temporal evolution of the time POD modes $\overline{\psi^v_{N_c^v}}$ and $\overline{\psi^w_{N_c^w}}$ are indistinguishable [Fig. 7(d)], indicating a very similar temporal evolution of the flow structures that correspond to the spatial POD modes $\overline{\phi^v_{N_c^v}}$ and $\overline{\phi^w_{N_c^w}}$, respectively; however, the energy contribution of the individual POD mode may differ. On the other hand, the turnover time of $\overline{\psi^u_{N_c^u}}$ (the cutoff time POD mode of the streamwise velocity) is approximately double when compared with $\overline{\psi^v_{N_c^v}}$ and $\overline{\psi^w_{N_c^w}}$ modes [Fig. 7(d)], indicating slower temporal evolution of the corresponding flow structures at the filter cutoff. Although this is a short-time flow dynamics, the proper orthogonal decomposition dictates the separation of scales as well as the time invariance of $\overline{\phi^i_{N_c^i}}$ and space invariance of $\overline{\psi^i_{N_c^i}}$ over the time duration of Δ_t. More details on the short-time snapshot POD in a parallel computing environment as well as a procedure to estimate the highest resolved POD modes and corresponding eddy turnover time are provided in Appendix B, where the high-energy lower-rank POD modes are also presented.

The necessary statistical properties of the total subfilter-scale stress tensor are laid out in Meneveau [89] in terms of the real (filtered) flow and subfilter-scale stress tensor. The time-averaged total subfilter-scale tensor $\langle \tau_{ij} \rangle^+$ as well as the Leonard $\langle \mathcal{L}_{ij} \rangle^+$, cross $\langle \mathcal{C}_{ij} \rangle^+$, and Reynolds $\langle \mathcal{R}_{ij} \rangle^+$ subfilter-scale stress tensors are displayed in Fig. 8. The total subfilter-scale stress tensor of Fig. 8(a) exhibits a close similarity with the Reynolds stress tensor obtained by using the time-averaging filter [Figs. 1(b)–1(e)], in terms of the profiles, relative magnitudes and the peak locations of the stresses. On the contrary, the DSM and WALE models do not exhibit such similarity for all the stress components (not shown). As anticipated, the diagonal terms of the Leonard ($\langle \mathcal{L}_{ii} \rangle^+$) and Reynolds ($\langle \mathcal{R}_{ii} \rangle^+$) subfilter-scale stress tensors mainly contribute to the diagonal terms $\langle \tau_{ii} \rangle^+$ of the total subfilter-scale stress tensor, whereas the cross subfilter-scale stress component $\langle \mathcal{C}_{12} \rangle^+$ [Fig. 8(d)] predominantly contributes to the off-diagonal term $\langle \tau_{12} \rangle^+$. The space or time integration of the diagonal stresses of cross subfilter-scale stress tensor must be zero due to the bi-orthogonality of the POD modes [50].

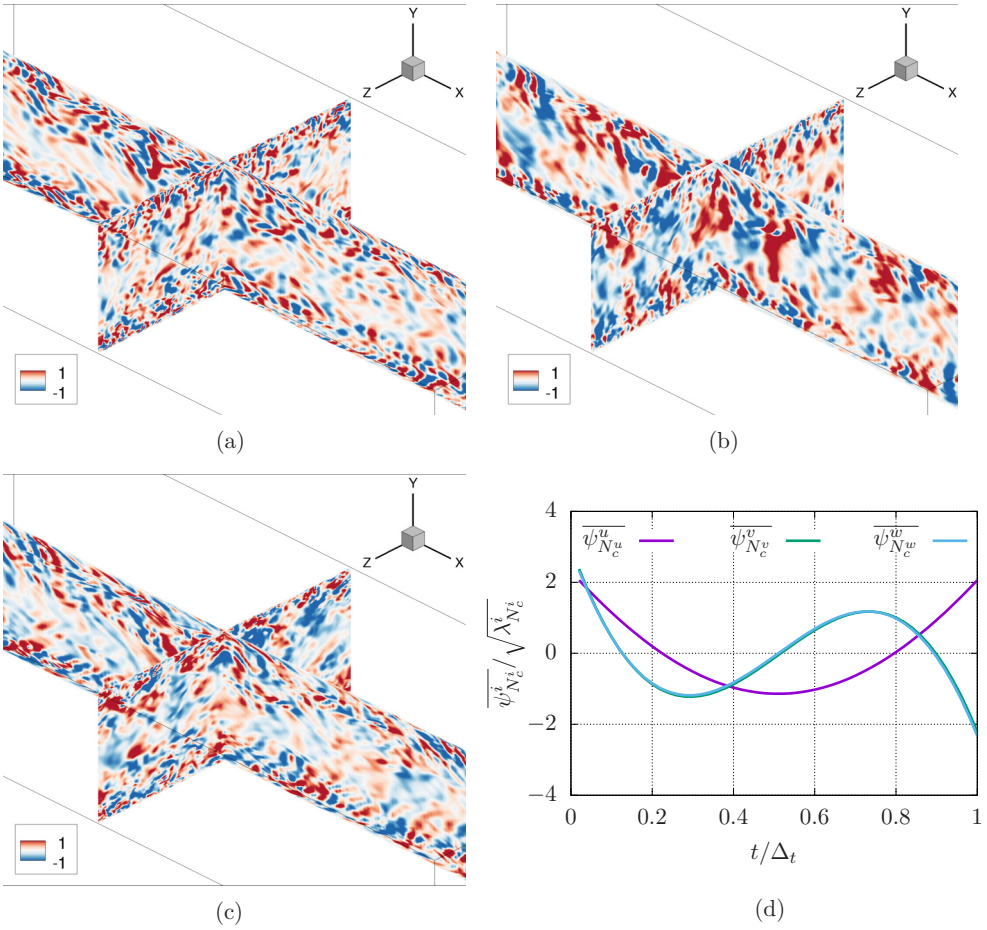

FIG. 7. The highest resolved POD modes at a time instance: (a) $\overline{\phi^u_{N_c^u}}$, (b) $\overline{\phi^v_{N_c^v}}$, (c) $\overline{\phi^w_{N_c^w}}$, (d) $\overline{\psi^i_{N_c^i}}$.

The scale similarity models are known for their appropriate behavior in different flow regimes. For instance, in the near-wall region, it is desired to have correct near-wall scaling of the modeled subfilter-scale stresses; particularly, the most relevant component, τ_{12} [16,90]. The near-wall scaling for the components of exact subfilter-scale stress tensor can be obtained by performing a Taylor-series expansion of the velocity in the wall normal direction, which leads to

$$\tau_{11} \sim y^2, \quad \tau_{22} \sim y^4, \quad \tau_{33} \sim y^2, \quad \tau_{12} \sim y^3, \quad \tau_{13} \sim y^2, \quad \tau_{23} \sim y^3. \tag{45}$$

As discussed in Liu, Meneveau, and Katz [32], the DSM exhibits accurate near-wall scaling only for τ_{12} and τ_{23}, predicting inaccurate near-wall behavior for the other components of subfilter-scale stresses. The near-wall behavior of the PODA model in terms of τ_{11}, τ_{22}, τ_{33}, and τ_{12} is shown in Fig. 8(e), where the subfilter-scale stresses exhibit the accurate near-wall scaling of Eq. (45). Similarly in the other regions of the flow, the PODA model is expected to manifest good correlations with the exact subfilter-scale stress tensor.

In the scale similarity model of Bardina [35], the subfilter-scale stress tensor has been modeled by using a Leonard subfilter-scale stress like term [which becomes Leonard subfilter-scale stress of Eq. (8) for $\overline{u_i u_j} \approx \overline{\overline{u_i}\,\overline{u_j}}$], ignoring the cross and Reynolds subfilter-scale stresses. The model locally led to better correlations with actual subfilter-scale stresses, but did not dissipate energy, promoting the development of mixed models [1,35]. The PODA model leverages the properties of POD, where

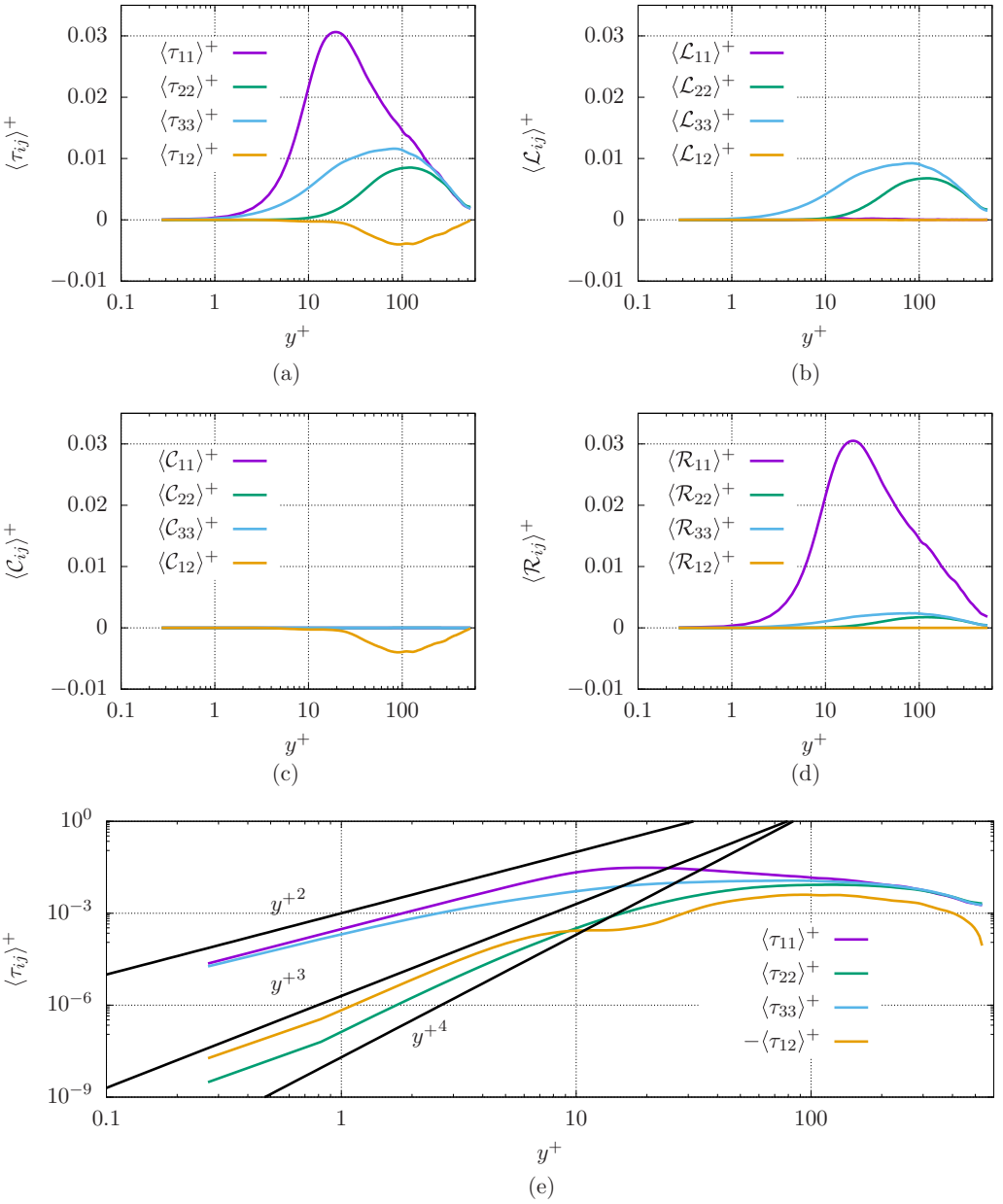

FIG. 8. Time-averaged components of subfilter-scale stress tensors and the near-wall scaling of total subfilter-scale stress tensor. (a) Total subfilter-scale stresses. (b) Leonard subfilter-scale stresses. (c) Cross subfilter-scale stresses. (d) Reynolds subfilter-scale stresses. (e) Near-wall scaling of the total subfilter-scale stresses.

the flow is decomposed into linearly uncorrelated modes, leading to better capturing of the cross and Reynolds subfilter-scale stresses in terms of POD modes. As shown in Fig. 8, the cross subfilter-scale stress mainly contributes to the deviatoric components of the total subfilter-scale stress, while Reynolds subfilter-scale stress represents a significant fraction of the total subfilter-scale stress. Consequently, the PODA model appears to be dissipative enough to accommodate the large energy backscatter of Figs. 3(b) and 4.

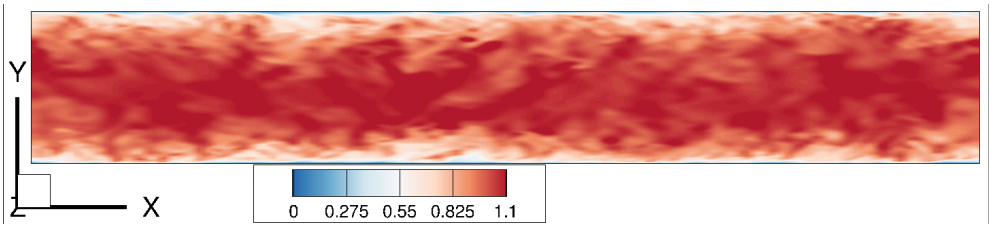

(a)

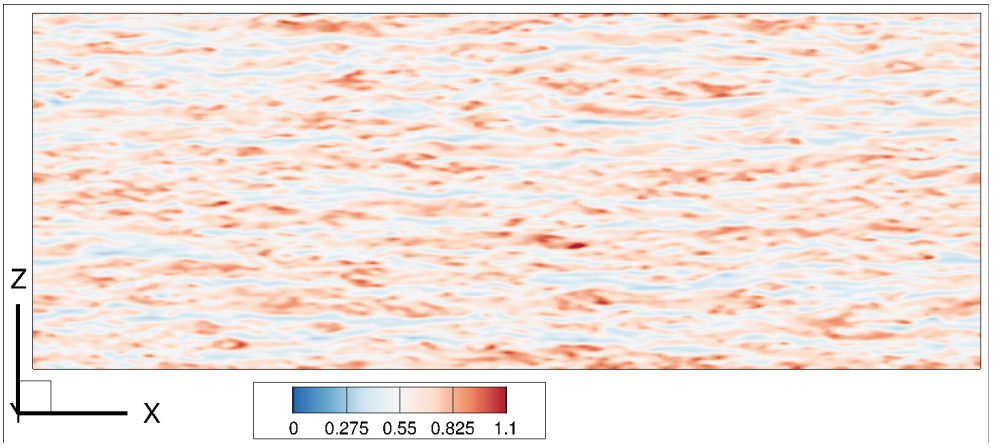

(b)

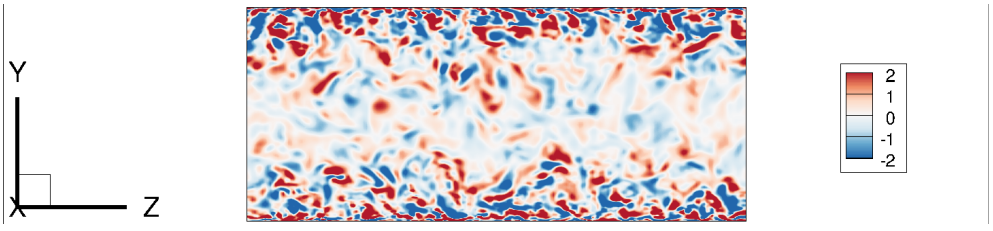

(c)

FIG. 9. Instantaneous flow fields by using PODA model. (a) Velocity magnitude ($||u||/u_b$) in XY plane at $z/h = 0$. (b) Velocity magnitude ($||u||/u_b$) in XZ plane at $y^+ = 18.11$. (c) Streamwise vorticity ($\omega_x h/u_b$) in YZ plane at $x/h = 2\pi h$.

The instantaneous flow fields in terms of the velocity magnitude and streamwise vorticity are shown in Fig. 9. The velocity magnitude $||u||$, normalized by the bulk velocity u_b, is shown in an XY plane (at $z/h = 3\pi/4$) and a horizontal XZ plane at $y^+ = 18.11$ ($y/h = 0.034$) in Figs. 9(a) and 9(b), respectively. The XZ plane [Fig. 9(b)] is located in the buffer layer and shows the near-wall streamwise elongated flow structures. The normalized streamwise vorticity $\omega_x h/u_b$ is shown in a YX plane at location $x = 2\pi h$ in Fig. 9(c), exhibiting the turbulent vortical structures.

B. Decaying isotropic turbulence

In this section, we consider a test case of the decaying isotropic turbulence. The LES are performed based on the experimental data of Comte-Bellot and Corrsin [86], referred to as CBC. In this experiment, a grid turbulence is generated by using a grid of size $M = 5.08 \times 10^{-2}$ m in a flow with the mean flow velocity of $U_o = 1000 \times 10^{-2}$ m/s. The decaying isotropic turbulence

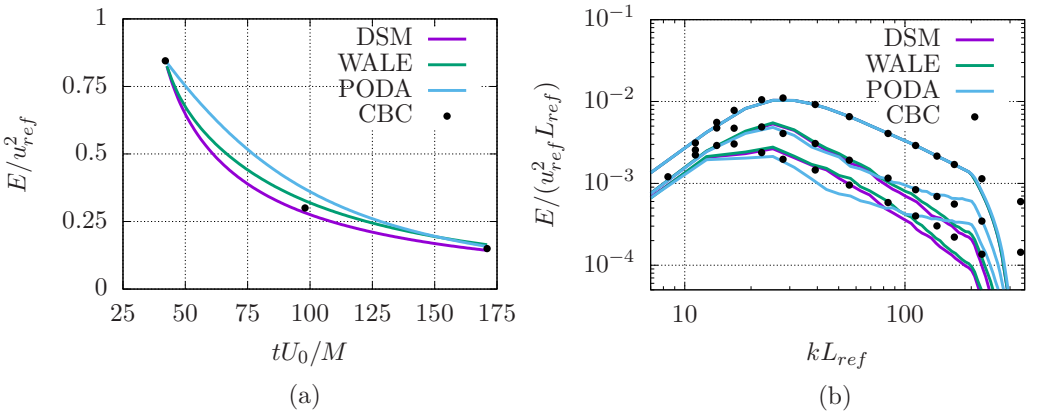

FIG. 10. Decaying isotropic turbulence. (a) Decay of total kinetic energy. (b) Energy spectra at the three stations.

is measured at $42M$, $98M$, and $171M$ downstream of the grid in terms of the second-order turbulence statistics, including energy spectra. The streamwise evolution of temporally stationary grid turbulence resembles the time evolution of an ideal isotropic turbulence, whose statistical properties are invariant under all axes rotations and reflections. Thus, simulation of a time evolving isotropic turbulence in a cubical box should match the experiment at $t = 42M/U_o$, $t = 98M/U_o$, and $t = 171M/U_o$, respectively, when started with an initial condition of turbulence at the grid location. Equivalently, for an initial condition of turbulence at the first location ($42M$), the results are expected to match for second ($98M$) and third ($171M$) locations at $t = 56M/U_o$ and $t = 129M/U_o$, respectively. The experimental data are nondimensionalized by using the reference velocity and length scales; where the reference length scale considered is $L_{\text{ref}} = 11M$, in order to accommodate approximately four integral scales [91]. The reference velocity u_{ref} is based on the measured velocity fluctuations at the first location, given as $u_{\text{ref}} = \sqrt{3\langle u_x' u_x' \rangle/2} = 27.19 \times 10^{-2}$ m/s.

The LES computations are preformed on a unit cube that is discretized in 64 cells in each direction, and a dimensionless time step of $1.594\,32 \times 10^{-3}$. The Reynolds number based on the size of the computational domain is $Re = 101\,29$, similar to Rozema *et al.* [92]. The decaying isotropic turbulence is simulated by using the presented subfilter-scale PODA model as well as the DSM and WALE models. In DSM simulations, the Smagorinsky constant is estimated by averaging the numerator and denominator of Eq. (15) in all the homogeneous directions. The simulations are initialized by using the experimental velocity spectrum at the first location, where the one-dimensional energy spectrum is assumed to be the radial three-dimensional spectrum due to the isotropy. The initial velocity field is generated by the energy spectrum and random phases, which requires a synchronization of the phase information. Thus, a precursor simulation is performed from $t = 0M/U_o$ to $t = 42M/U_o$, and the resulting velocity field is adjusted [93], providing a new initial condition at $t = 42M/U_o$.

The decay of total turbulent kinetic energy predicted by the three models alongside the experimental results of CBC are displayed in Fig. 10(a). The isotropic turbulence in the simulations, starting with an initial condition based on the first station ($42M$), is allowed to decay from $t = 42M/U_o$ to $t = 171M/U_o$. In general, the three models accurately predict the turbulent kinetic energy at the last station ($171M$) [Fig. 10(a)]; however, the rates of energy decay differ among the models, particularly between the first and second stations. The LES predictions of the energy spectra at the two downstream stations, $t = 98M/U_o$ and $t = 171M/U_o$, are compared with the experimental results in Fig. 10(b). As expected, the DSM and WALE models provide sufficient dissipation near the filter cutoff wave number, whereas the PODA model is less dissipative, as was observed for the turbulent channel flow in Fig. 3(a). The energy spectra for the DSM exhibit a good match with

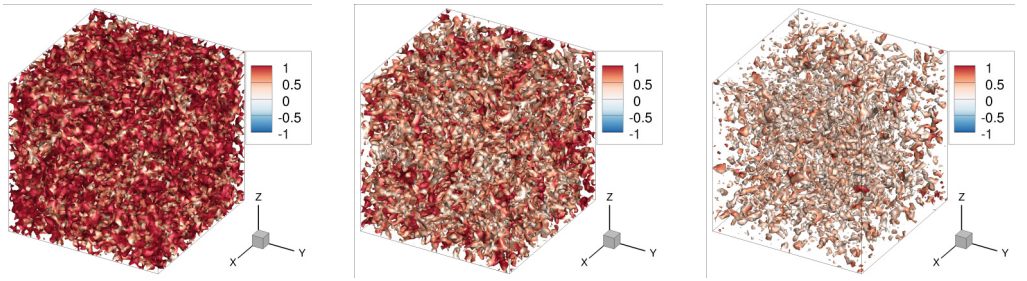

FIG. 11. Decaying isotropic turbulence at different times, in terms of Q criterion isosurface ($Q = 150$) colored with velocity magnitude by using PODA model. (a) $tU_0/M = 42$. (b) $tU_0/M = 98$. (c) $tU_0/M = 171$.

box-filtered experimental data, as shown in Rozema *et al.* [92]. The temporal evolution and spectral energies predicted by the WALE model are slightly higher when compared with the DSM model; a similar trend was also observed by Toda, Truffin, and Nicoud [21]. The PODA model shows better agreement with the unfiltered experimental data, due to its lower dissipation; however, the energy spectra exhibit some discrepancies in the spectral energy profile at the third station ($171M$), particularly for $kL_{\text{ref}} \approx 50$ and near the filter cutoff wave number.

The three-dimensional flow fields of decaying isotropic turbulence are displayed in Fig. 11 for the three time instances $tU_0/M = 42$ [Fig. 11(a)], $tU_0/M = 98$ [Fig. 11(b)], and $tU_0/M = 171$ [Fig. 11(c)], which correspond to the three stations of the CBC experiment, $42M$, $98M$, and $171M$, respectively. The figures show Q criterion, defined as $Q = 1/2(\Omega_{ij}\Omega_{ij} - S_{ij}S_{ij})$, isosurface for $Q = 150$ and colored by velocity magnitude, indicating the decay of three-dimensional flow structures for the increase of time.

V. CONCLUSION

This article presents a proper orthogonal decomposition (POD) assisted approach of subfilter-scale turbulence modeling for large eddy simulations (LES). The subfilter-scale stress tensors (Leonard, cross, and Reynolds tensors) are directly expressed in terms of POD modes, in their complete form. The cross and Reynolds subfilter-scale tensors, which comprise the subfilter scales, are modeled by means of high-rank low-energy resolved POD modes, assuming the scale similarity of turbulence. The scale similarity is also used to estimate the energy transfer between the resolved and subfilter scales, leading to a flow- and filter-specific model parameter computed on the fly. The POD-assisted (PODA) model naturally exhibits the correct near-wall scaling as well as the backscatter of subfilter-scale energy. The features of the PODA model are discussed by simulating two canonical test cases: the turbulence channel flow and decaying isotropic turbulence, in comparison with the dynamic Smagorinsky model (DSM) and wall-adapting local eddy-viscosity (WALE) models of LES. The computational cost overhead is $\approx$12% compared with the DSM, which can be reduced by efficiently handling the data. In addition to the computational efficiency and application to complex turbulent flows, the PODA modeling approach can be conveniently leveraged for the modeling of subfilter-scale stresses in multiphysics flows.

ACKNOWLEDGMENTS

The author would like to express gratitude to Prof. Datta Gaitonde for his guidance, and granting access to the Ohio Supercomputing Center (OSC). The author acknowledges anonymous reviewers for their suggestions.

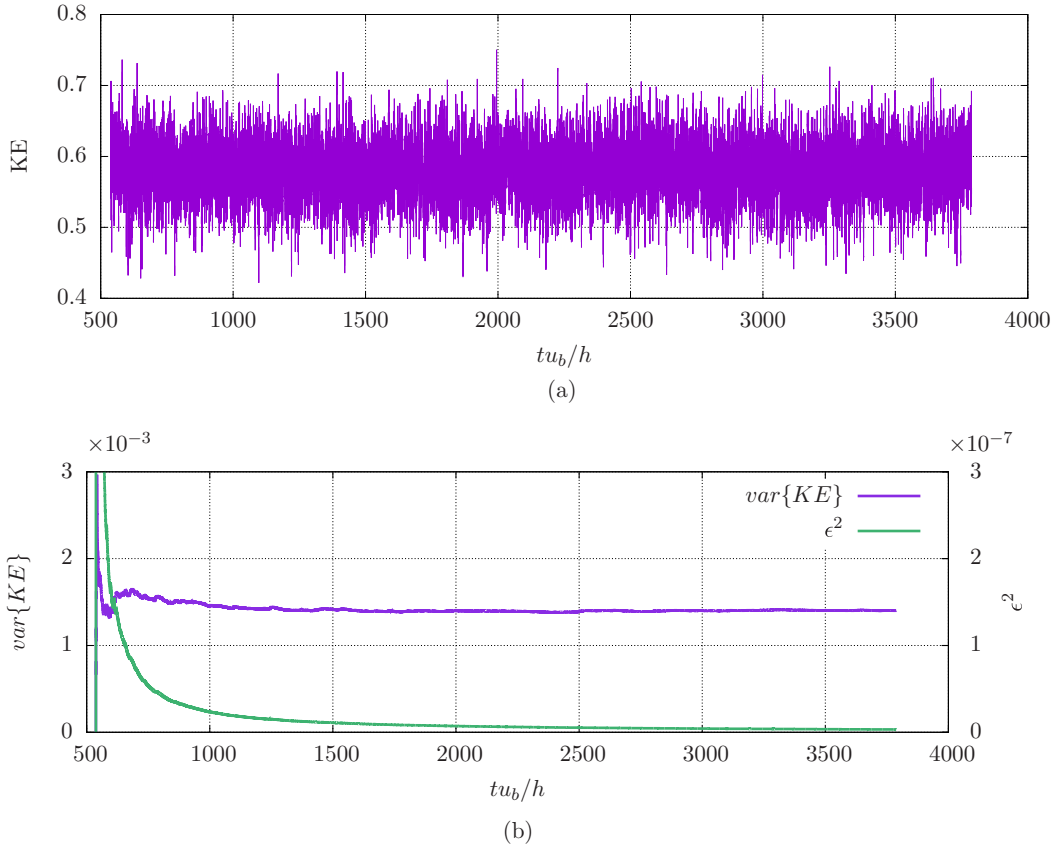

FIG. 12. Total kinetic-energy statistics. (a) Time signal of total kinetic energy at ($x/h = 2\pi$, $y/h = 1$, $z/h = 3\pi/4$). (b) Variance and variability of the total kinetic energy versus time.

APPENDIX A: STATISTICAL CONVERGENCE OF RESULTS

The uncertainty in the stationary flow statistics of high-fidelity simulations, e.g., direct numerical simulations (DNS), large eddy simulations (LES), is crucial; particularly where experimental results are not available [94]. In addition to parameters such as the computational domain extents, discretization errors, nonuniqueness of the statistically stationary state, and numerical methods, the statistical errors can cause some discrepancies in the turbulent flow statistics for the same flow conditions [95]. A first step in the statistical convergence analysis is to identify the initial transient response time and the stationary response time. The initial transient time for the turbulent channel flow DNS is usually estimated in terms of the linear profile of total shear stress and quasiperiodic total kinetic energy (KE) [96,97]. The flow stationarity, on the contrary, is often loosely defined; Moser, Kim, and Mansour [97] considered the turbulent channel flow to be stationary for $t \geqslant 10L_x/u_b$, based on their prior experience.

A stationary response of the total kinetic energy (KE) is shown in Fig. 12(a) for the LES performed using the proper orthogonal decomposition assisted (PODA) model, where the KE is probed at $x/h = 2\pi, y/h = 1, z/h = 3\pi/4$, inside the computational domain described in Sec. IV A. The temporal evolution of the KE exhibits an initial transient of $tu_b/h \approx 100$, which approximately corresponds to the above estimate of $t \geqslant 10L_x/u_b$ by Moser, Kim, and Mansour [97] for their DNS. The variance of the KE with increasing time, Fig. 12(b), indicates the initial transient and convergence to a stationary response. The variance can be estimated by using a discrete temporal

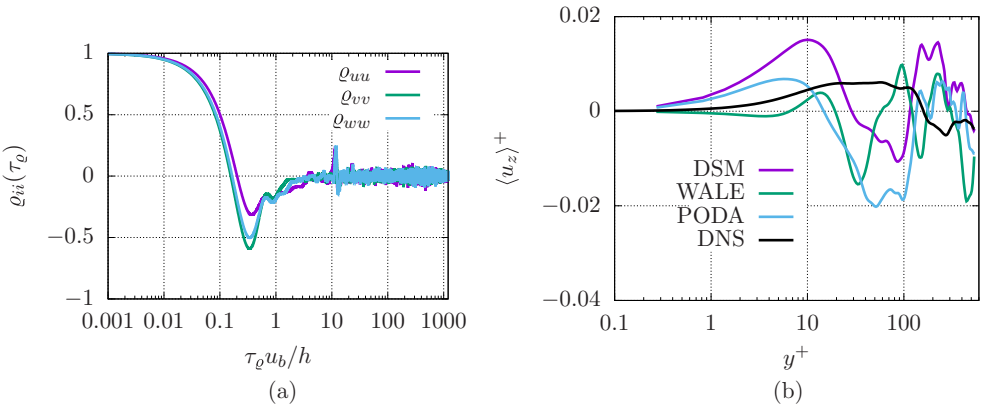

FIG. 13. Temporal autocorrelations of the velocity components and the time-averaged spanwise velocity. (a) Autocorrelations of the velocity components. (b) $\langle u_z \rangle^+$ for the three LES and DNS.

data as

$$var\{KE\} = \frac{1}{N}\sum_{n=1}^{N}(KE_n - \langle KE \rangle)^2, \tag{A1}$$

where $\langle KE \rangle$ is the time averaged kinetic energy (KE), which also reaches a stationary state for increasing time (not shown). N denotes the number of samples. A measure of convergence in terms of the variability, ϵ, can be given as

$$\epsilon^2 = \frac{1}{N}\frac{var\{KE\}}{\langle KE \rangle^2}, \tag{A2}$$

which can provide an estimate of the smallest N for a given level of fluctuations in KE. Figure 12(b) shows the variability of KE estimated using Eq. (A2).

As noted earlier, the LES statistics are gathered after the initial transient and for ≈240 flow-through times. The spatial and temporal extents of the large eddies in the flow can be obtained in terms of the space and/or time autocorrelations of the flow variables. The temporal autocorrelations for the three velocity components at the probe location ($x/h = 2\pi, y/h = 1, z/h = 3\pi/4$) are shown in Fig. 13(a), which are given as

$$\varrho_{ii}(\tau_\varrho) = \frac{\langle u_i'(t)u_i'(t+\tau_\varrho)\rangle}{\langle u_i'(t)u_i'(t)\rangle}. \tag{A3}$$

The Wiener-Khinchin theorem allows us to estimate the autocorrelation in an efficient way by using a fast Fourier transform (FFT) as

$$\mathcal{F}_i(f) = FFT\{u_i'(t)\}, \tag{A4}$$

$$\mathcal{S}_{ii}(f) = \mathcal{F}_i(f)\mathcal{F}_i^*(f), \tag{A5}$$

$$\varrho_{ii}(\tau_\varrho) = IFFT\{\mathcal{S}_{ii}(f)\}, \tag{A6}$$

where IFFT denotes the inverse FFT. $\mathcal{F}^*$ is the complex conjugate of $\mathcal{F}(f)$, while $\mathcal{S}_{ii}(f)$ represents the power spectral density of the velocity fluctuation $u_i'(t)$. At first, the normalized autocorrelations [Fig. 13(a)] decrease monotonically following a Gaussian profile and become negative at $\tau_\varrho u_b/h \approx 0.2$. The negative correlations gradually increase to zero at $\tau_\varrho u_b/h \approx 3$, which indicates that the correlation or turnover time of the large eddies is ≈3, resulting in ≈1000 turnovers of the large

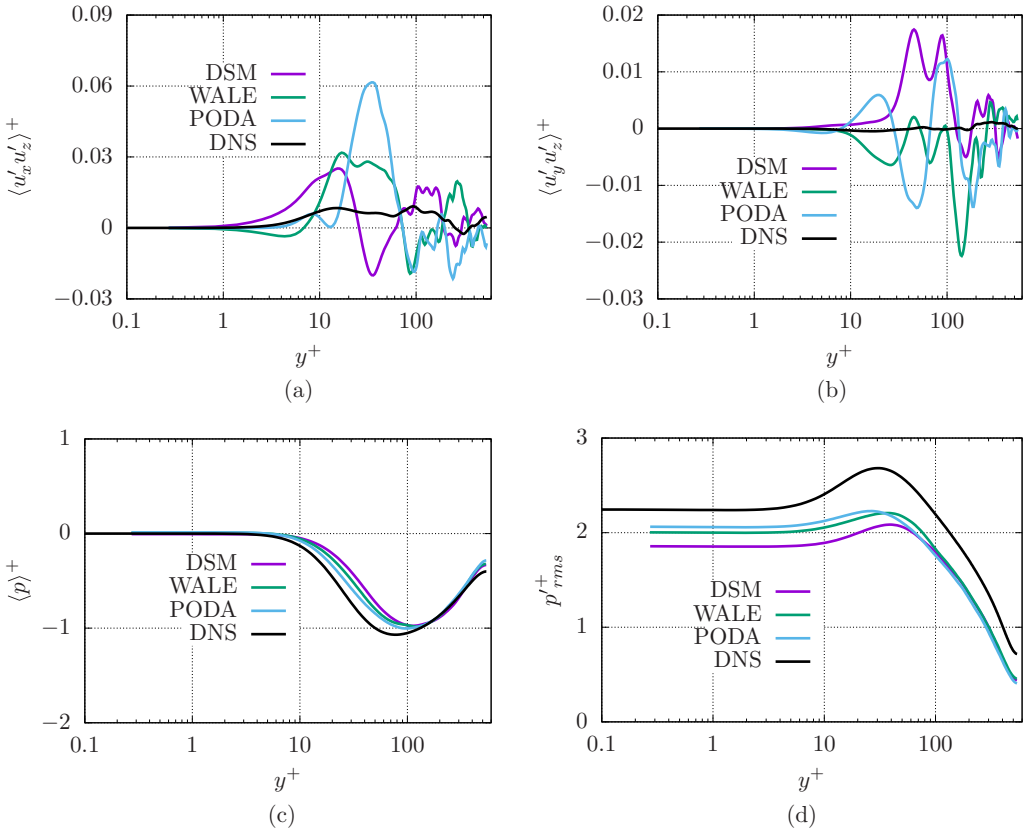

FIG. 14. Comparison of the time-averaged Reynolds stress deviatoric components and pressure profiles between the LES and DNS. (a) Reynolds stress component comprising the x and z velocity fluctuations. (b) Reynolds stress component comprising the y and z velocity fluctuations. (c) Time-averaged pressure. (d) Root-mean-squared (rms) pressure fluctuations.

flow structures for the estimation of statistics. The correlations [Fig. 13(a)] also exhibit peaks at $\tau_\varrho u_b/h \approx 12$, which appears to be due to the streamwise periodicity, of 4π, of the computational domain.

The turbulent channel flow is homogeneous in the spanwise direction with zero mean flow, thus the time-averaged spanwise velocity provides an indication of numerical convergence. Figure 13(b) shows the time-mean spanwise velocity, $\langle u_z \rangle^+$, for the LES using the three models along with the DNS. Similar to the DNS profile, the LES profiles manifest peaks of $\langle u_z \rangle^+$ near the buffer or log-layer regions of the boundary layer ($10 \lessapprox y^+ \lessapprox 500$); however, the magnitudes of spanwise velocity are ≈4 to 6 times higher for the LES computations when compared with the DNS.

To further assess the results convergence, we compare the deviatoric Reynolds stress components and pressure profiles along the wall normal direction between the three LES and DNS. The comparison is displayed in Fig. 14. The Reynolds stress components $\langle u'_x u'_z \rangle^+$ and $\langle u'_y u'_z \rangle^+$ are shown in Figs. 14(a) and 14(b), respectively, exhibiting discrepancies between the LES and DNS profiles mainly in the $10 \lessapprox y^+ \lessapprox 100$ range. For the LES as well as DNS, $\langle u'_x u'_z \rangle^+$ is higher than $\langle u'_y u'_z \rangle^+$, due to the higher magnitude of streamwise velocity fluctuations.

The time-averaged pressure and root-mean-squared (rms) pressure fluctuations along the wall normal direction are compared between the LES and DNS in Figs. 14(c) and 14(d), respectively. The pressure profiles, $\langle p \rangle^+$ and p'^+_{rms}, are normalized by using the friction velocity u_τ as $\langle p \rangle^+ = \langle p \rangle / u_\tau^2$

and $p'^{+}_{\mathrm{rms}} = p'_{\mathrm{rms}}/u_\tau^2$. The mean-pressure profiles for the LES show a good agreement with the DNS profile [Fig. 14(c)] with some discrepancies in the $10 \lessapprox y^+ \lessapprox 100$ range; whereas the LES predictions of the rms pressure fluctuations by using the three LES models show a reasonable match with the DNS profile [Fig. 14(d)]. For both the pressure profiles, the PODA model predictions are in a better agreement with the DNS results when compared with the DSM and WALE models.

APPENDIX B: SHORT-TIME SNAPSHOT PROPER ORTHOGONAL DECOMPOSITION

As discussed in Sec. II, the classical proper orthogonal decomposition (POD) and its variants, in general, use long-time stationary flow data in order to educe time-invariant modes. The snapshot POD procedure [67] considers a number of flow fields and leads to equal numbers of POD modes. The first POD mode represents the time average of the considered flow fields, while the remaining POD modes represent the fluctuating part of the flow fields. For a stationary flow, the first POD time mode (temporal coefficient) must remain constant over the time, whereas for a nonstationary flow, it may vary with time. The low rank energy dominant POD modes (e.g., mode no. 2, 3) provide dominant unsteadiness, particularly for the time-periodic flows (e.g., flow past a cylinder). The snapshot POD has been successfully used for nonstationary flows [98], where the classical POD is extended for a short-time flow realizations. For periodic flows, a short-time snapshot POD analysis can be performed on as small as one period of the flow, yet it leads to POD modes almost identical to the modes obtained by considering a large number of flow periods [99,100].

In the present approach, the time duration of the snapshots collection is equal to the turnover time of the smallest resolved eddies, i.e., Δ_t. Thus for a constant time step of simulation, δt, the number of snapshots, N_t, to perform POD becomes

$$N_t = \frac{\Delta_t}{\delta t}. \tag{B1}$$

In a parallel computing environment, each central processing unit (CPU) locally stores N_t number of snapshots, leading to sets of N_t time-evolving flow fields of the partial computational domains. At first, a time-correlation matrix of size $N_t \times N_t$ is locally constructed; and then the summation of the local correlation matrices over all CPUs is performed in order to obtain a global time-correlation matrix of the same dimensions. Each processor then solves the global correlation matrix for an eigenvalue problem, obtaining an identical set of eigenvectors $\overline{e_n^i}(t_n)$ and eigenvalues λ_n^i. The real-symmetric correlation matrix is solved by using a standard Jacobi eigenvalue algorithm [101]. The POD space modes on each processor are obtained by using the partial flow fields and eigenvectors as

$$\overline{\Phi_n^i}(\boldsymbol{x}_l|\boldsymbol{x}_l \subset x) = \frac{1}{\sqrt{N_t}}\left(\overline{u_i}(\boldsymbol{x}_l|\boldsymbol{x}_l \subset x, \cdot), \overline{e_n^i}(\cdot)\right)_{\Delta_t}, \tag{B2}$$

$$\overline{\phi_n^i}(\boldsymbol{x}_l|\boldsymbol{x}_l \subset x) = \overline{\Phi_n^i}(\boldsymbol{x}_l|\boldsymbol{x}_l \subset x)/||\overline{\Phi_n^i}(\boldsymbol{x})||, \tag{B3}$$

where $\boldsymbol{x}_l$ is a partial computational domain on a CPU. The Euclidean $\boldsymbol{L}^2$ norm $||\cdot||$ is computed on the total computational domain $\boldsymbol{x}$. The standard inner product in terms of arbitrary variables a and b is defined as

$$(a, b)_{\mathcal{D}} = \int_{\mathcal{D}} a \cdot b\mathcal{W} d\boldsymbol{x} \text{ or } (a, b)_{\mathcal{D}} = \int_{\mathcal{D}} a \cdot b dt, \tag{B4}$$

where $\mathcal{D}$ is the space or time domain for the inner product, while $\mathcal{W}$ denotes the weights of nonuniform computational grid. Thus, the norm is given as

$$||a|| = \sqrt{(a, a)_{\mathcal{D}}}. \tag{B5}$$

By using the partial orthonormal POD space modes, the time modes are obtained as,

$$\overline{\psi_n^i}(t) = \left(\overline{\phi_n^i}(\cdot), \overline{u_i}(\cdot, t)\right)_{\boldsymbol{x}_l}. \tag{B6}$$

An algorithm (Algorithm 1) to perform the short-time snapshot POD is provided below:

Algorithm 1: Short-time snapshot POD

Input:	$\overline{u_i}(\boldsymbol{x}, t) \in \mathbb{R}^{N_x \times N_t}$
Output:	$\overline{\phi_n^i}(\boldsymbol{x}) \in \mathbb{R}^{N_x}$, $\overline{\psi_n^i}(t) \in \mathbb{R}^{N_t}$, λ_n^i
	# Construct a local time-correlation matrix on each processor
1:	$\mathsf{C}_l = \left(\overline{u_i}(\cdot, t), \overline{u_i}^*(\cdot, t)\right)_{\boldsymbol{x}_l}, \quad \mathsf{C}_l \in \mathbb{R}^{N_t \times N_t}$
	# Construct a global time-correlation matrix on each processor
2:	$\mathsf{C}_g = \sum_l \mathsf{C}_l, \quad \mathsf{C}_g \in \mathbb{R}^{N_t \times N_t}$
	# Solve C_g for eigenvectors and eigenvalues using iterative Jacobi eigenvalue algorithm (convergence criterion: 10^{-8})
3:	$C_g \overline{e_n^i} = \lambda_n^i \overline{e_n^i}, \quad \overline{e_n^i}(t) \in \mathbb{R}^{N_t}$
	# Compute the orthogonal space modes on partial spatial domain
4:	$\overline{\Phi_n^i}(\boldsymbol{x}_l) = \frac{1}{\sqrt{N_t}} \left(\overline{u_i}(\boldsymbol{x}_l, \cdot), \overline{e_n^i}(\cdot)\right)_{\Delta_t}, \quad \overline{\Phi_n^i}(\boldsymbol{x}_l) \in \mathbb{R}^{N_{x_l}}$
	# Compute the partial orthonormal space modes using a global norm
5:	$\overline{\phi_n^i}(\boldsymbol{x}_l) = \overline{\Phi_n^i}(\boldsymbol{x}_l)/\|\overline{\Phi_n^i}(\boldsymbol{x})\|, \quad \overline{\phi_n^i}(\boldsymbol{x}_l) \in \mathbb{R}^{N_{x_l}}$
	# Compute the orthogonal time POD modes
6:	$\overline{\psi_n^i}(t) = \left(\overline{\phi_n^i}(\cdot), \overline{u_i}(\cdot, t)\right)_{\boldsymbol{x}_l}, \quad \overline{\psi_n^i}(t) \in \mathbb{R}^{N_t}$
	# Compute complete spatial modes if needed (e.g., for postprocessing)
7:	$\overline{\phi_n^i}(\boldsymbol{x}) = \overline{\phi_n^i}(\sum_l \boldsymbol{x}_l), \quad \overline{\phi_n^i}(\boldsymbol{x}) \in \mathbb{R}^{N_x}$

The results of short-time snapshot POD analysis for an intermediate stage are presented in Figs. 15 and 16 for simulation using mesh M1 (refer to Table III). The average turnover time of the smallest resolved eddies for mesh M1 is $\langle \Delta_t \rangle^+ = 1.0369$ (Table IV); for a simulation time step of $(\delta t) u_b/h = 0.0025$, the average number of snapshots used for the short-time snapshot POD gives $\langle N_t \rangle \approx 14$. For the presented POD modes, the number of snapshots obtained were $N_t = 50$, leading to three resolved POD modes for the streamwise velocity component, and four resolved POD modes for the spanwise and wall normal velocity components. The orthonormal space modes, $\overline{\phi_n^i}(\boldsymbol{x})$, are displayed in Fig. 15, where the Fig. 15(g) shows the cutoff mode for the streamwise velocity. The cutoff modes for the wall normal and spanwise velocity components are shown in Figs. 7(b) and 7(c), respectively. The first POD mode $\overline{\phi_1^u}$ [Fig. 15(a)] corresponds to the streamwise flow velocity, indicating the mean flow, $\langle u_x \rangle_{\Delta_t}$, in the short-time sense; similarly, modes $\overline{\phi_1^v}$ [Fig. 15(b)] and $\overline{\phi_1^w}$ [Fig. 15(c)] represent the short-time mean flow in the wall normal and spanwise directions, respectively. The second and higher rank POD modes, e.g., Figs. 15(d) to 15(i), and the cutoff modes of Fig. 7, represent the decomposition of unsteady flow structures exhibited during the short-time window. It is evident from Fig. 15 that the sizes of the spatial POD modal structures (characteristic eddies) decrease for the higher rank POD modes for a particular component of the velocity.

The orthogonal temporal POD modes $\overline{\psi_n^i}(t)$, that are obtained using Eq. (B6), are shown in Figs. 16(a)–16(c) for the streamwise, wall normal, and spanwise velocity components, respectively. As anticipated, the temporal POD modes exhibit increased variations and oscillations for the higher-rank POD modes, an attribute analogous to their spatial counterparts $\overline{\phi_n^i}(\boldsymbol{x})$. The temporal modes dictate the time-varying contribution of the corresponding spatial POD modes to the flow field. Although the POD spatial modes are dissimilar for different velocity components, the temporal dynamics appears identical for the POD modes of the same rank. The eigenvalues λ_n^i of the resolved and a few high-rank POD modes are shown in Fig. 16(d), where the eigenvalues are normalized by λ_1^i. The energy contribution of the subfilter-scale modes, for the present example, is approximated

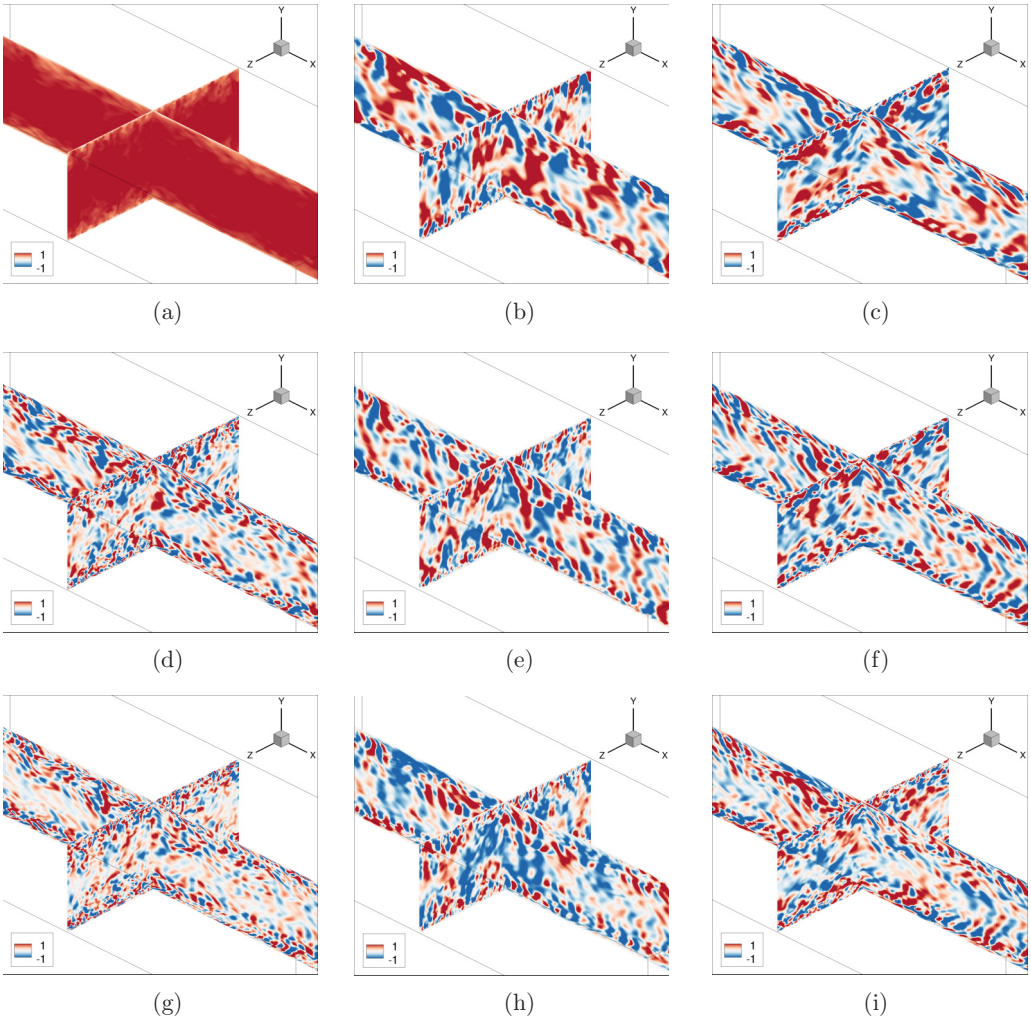

FIG. 15. Resolved POD space modes for the three velocity components: (a) $\overline{\phi_1^u}$, (b) $\overline{\phi_1^v}$, (c) $\overline{\phi_1^w}$, (d) $\overline{\phi_2^u}$, (e) $\overline{\phi_2^v}$, (f) $\overline{\phi_2^w}$, (g) $\overline{\phi_3^u}$, (h) $\overline{\phi_3^v}$, (i) $\overline{\phi_3^w}$.

in terms of the ratio λ_3^u/λ_2^u for the streamwise velocity and λ_4^i/λ_3^i for the wall normal and spanwise velocity components, as discussed in Sec. II, Eq. (30).

To obtain the highest resolved (cutoff) POD mode, the POD modal energies are, at first, estimated by using the short-time averaging: $\langle\overline{\psi_n^i}^2\rangle_{\Delta_t}$, and then compared with the corresponding eigenvalues λ_n^i; where Eq. (41) is satisfied for the resolved POD modes. Figure 17(a) shows the comparison between the modal energies for the streamwise velocity component, where the energies estimated by the two means are compared. The discrepancy in the energy values for the rank-4 POD mode is evident, making the rank-3 mode the highest resolved POD mode. A temporal autocorrelation of the cutoff POD time mode is performed in order to capture the turnover time of the corresponding eddies. In a similar effort, Pruett [102] estimated an autocorrelation of velocity in order to extract a temporal scale. Figure 17(b) shows the autocorrelation of the highest resolved POD mode for the spanwise velocity component, where the correlation is estimated by using the procedure described

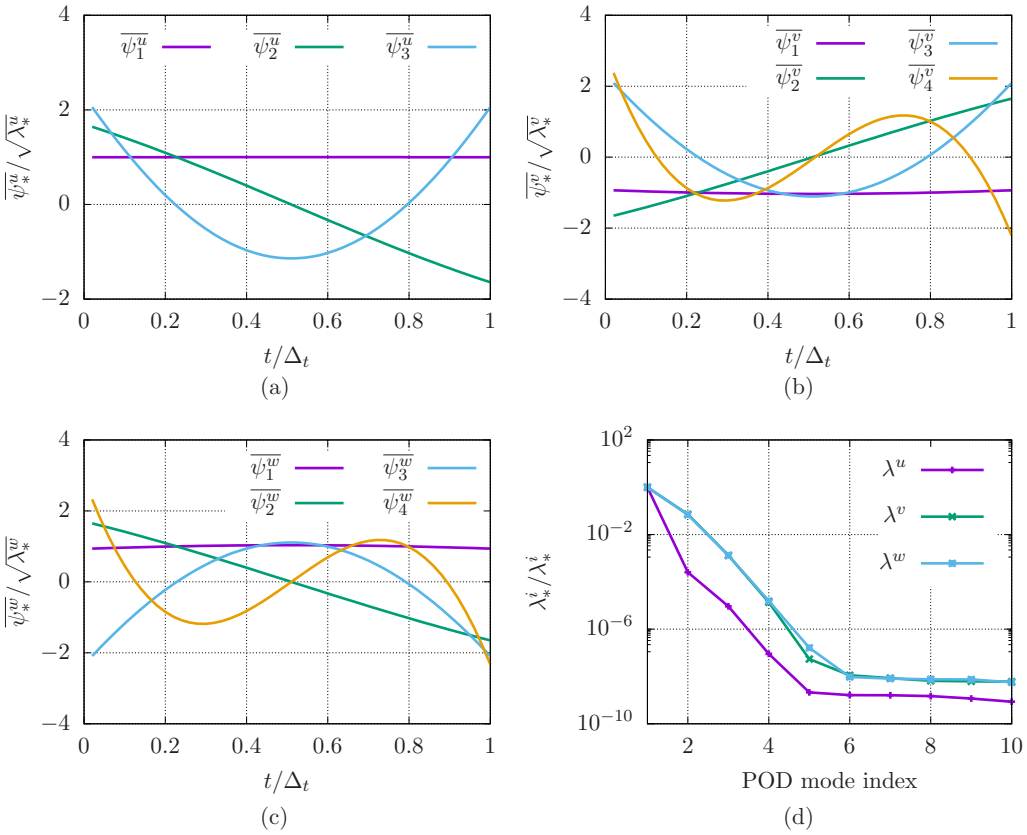

FIG. 16. POD time modes and associated eigenvalues. (a) POD time modes of streamwise velocity. (b) POD time modes of wall normal velocity. (c) POD time modes of spanwise velocity. (d) Eigenvalues of the POD modes.

in Appendix A. The eddy turnover time for the cutoff time POD mode of the streamwise velocity component is $\Delta_t \approx 0.128$; similarly an estimate of the eddy turnover time for the wall normal and spanwise components is ≈0.070, resulting in a fewer number of snapshots $N_t = 28$ for the next short-time POD.

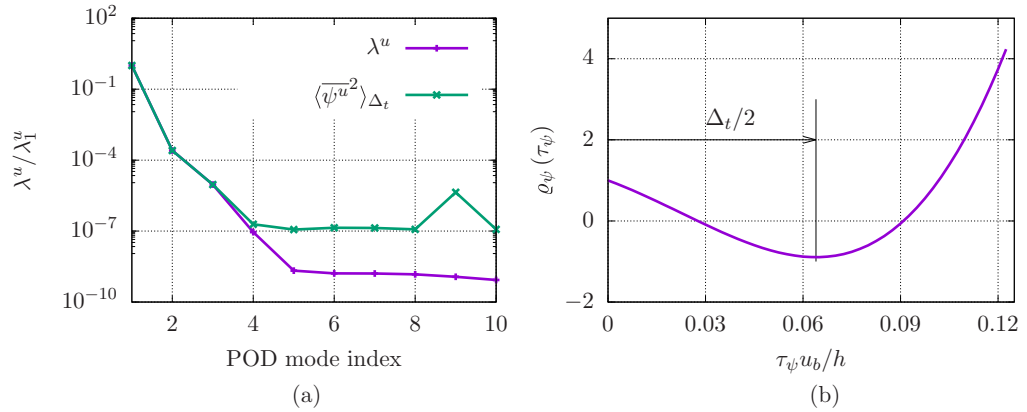

FIG. 17. Estimation of the cutoff POD mode and turnover time of the associated flow eddies.

[1] S. B. Pope, *Turbulent Flows* (Cambridge University Press, 2000).
[2] A. Leonard, Energy cascade in large-eddy simulations of turbulent fluid flows, in *Advances in Geophysics* (Elsevier, 1975), Vol. 18, pp. 237–248.
[3] R. A. Clark, J. H. Ferziger, and W. C. Reynolds, Evaluation of subgrid-scale models using an accurately simulated turbulent flow, J. Fluid Mech. **91**, 1 (1979).
[4] M. Germano, A proposal for a redefinition of the turbulent stresses in the filtered navier–Stokes equations, Phys. Fluids **29**, 2323 (1986).
[5] C. G. Speziale, Galilean invariance of subgrid-scale stress models in the large-eddy simulation of turbulence, J. Fluid Mech. **156**, 55 (1985).
[6] B. Vreman, B. Geurts, and H. Kuerten, Realizability conditions for the turbulent stress tensor in large-eddy simulation, J. Fluid Mech. **278**, 351 (1994).
[7] R. Mokhtarpoor and S. Heinz, Dynamic large eddy simulation: Stability via realizability, Phys. Fluids **29**, 105104 (2017).
[8] D. Leslie and G. Quarini, The application of turbulence theory to the formulation of subgrid modeling procedures, J. Fluid Mech. **91**, 65 (1979).
[9] J. R. Chasnov, Simulation of the Kolmogorov inertial subrange using an improved subgrid model, Phys. Fluids A **3**, 188 (1991).
[10] P. Sagaut, *Large Eddy Simulation for Incompressible Flows: An Introduction* (Springer Science & Business Media, Berlin, 2006).
[11] J. Smagorinsky, General circulation experiments with the primitive equations: I. The basic experiment, Mon. Weather Rev. **91**, 99 (1963).
[12] D. K. Lilly, The representation of small-scale turbulence in numerical simulation experiments, in *Proceedings of IBM Scientific Computing Symposium on Environmental Sciences*, edited by H. H. Goldstine (Yorktown Heights, New York, 1967), pp. 195–210.
[13] J. Deardorff, On the magnitude of the subgrid scale eddy coefficient, J. Comput. Phys. **7**, 120 (1971).
[14] P. Mason and N. Callen, On the magnitude of the subgrid-scale eddy coefficient in large-eddy simulations of turbulent channel flow, J. Fluid Mech. **162**, 439 (1986).
[15] Y. Zang, R. L. Street, and J. R. Koseff, A dynamic mixed subgrid-scale model and its application to turbulent recirculating flows, Phys. Fluids A **5**, 3186 (1993).
[16] M. Germano, U. Piomelli, P. Moin, and W. H. Cabot, A dynamic subgrid-scale eddy viscosity model, Phys. Fluids A **3**, 1760 (1991).
[17] D. K. Lilly, A proposed modification of the Germano subgrid-scale closure method, Phys. Fluids A **4**, 633 (1992).
[18] S. Ghosal, T. S. Lund, P. Moin, and K. Akselvoll, A dynamic localization model for large-eddy simulation of turbulent flows, J. Fluid Mech. **286**, 229 (1995).
[19] C. Meneveau, T. S. Lund, and W. H. Cabot, A Lagrangian dynamic subgrid-scale model of turbulence, J. Fluid Mech. **319**, 353 (1996).
[20] F. Nicoud and F. Ducros, Subgrid-scale stress modeling based on the square of the velocity gradient tensor, Flow, Turbul. Combust. **62**, 183 (1999).
[21] H. B. Toda, K. Truffin, and F. Nicoud, Is the dynamic procedure appropriate for all SGS models, in *V European Conference on Computational Fluid Dynamics, ECCOMAS, Lisbon, Portugal* (2010), pp. 14–17.
[22] K. Horiuti, A proper velocity scale for modeling subgrid-scale eddy viscosities in large eddy simulation, Phys. Fluids A **5**, 146 (1993).
[23] A. Vreman, An eddy-viscosity subgrid-scale model for turbulent shear flow: Algebraic theory and applications, Phys. Fluids **16**, 3670 (2004).
[24] N. Park, S. Lee, J. Lee, and H. Choi, A dynamic subgrid-scale eddy viscosity model with a global model coefficient, Phys. Fluids **18**, 125109 (2006).
[25] U. Piomelli, A. Rouhi, and B. J. Geurts, A grid-independent length scale for large-eddy simulations, J. Fluid Mech. **766**, 499 (2015).
[26] A. Rouhi, U. Piomelli, and B. J. Geurts, Dynamic subfilter-scale stress model for large-eddy simulations, Phys. Rev. Fluids **1**, 044401 (2016).

[27] B. Tao, J. Katz, and C. Meneveau, Statistical geometry of subgrid-scale stresses determined from holographic particle image velocimetry measurements, J. Fluid Mech. **457**, 35 (2002).
[28] M. H. Silvis, R. A. Remmerswaal, and R. Verstappen, Physical consistency of subgrid-scale models for large-eddy simulation of incompressible turbulent flows, Phys. Fluids **29**, 015105 (2017).
[29] M. V. Salvetti and S. Banerjee, A priori tests of a new dynamic subgrid-scale model for finite-difference large-eddy simulations, Phys. Fluids **7**, 2831 (1995).
[30] D. Carati, S. Ghosal, and P. Moin, On the representation of backscatter in dynamic localization models, Phys. Fluids **7**, 606 (1995).
[31] U. Schumann, Subgrid scale model for finite difference simulations of turbulent flows in plane channels and annuli, J. Comput. Phys. **18**, 376 (1975).
[32] S. Liu, C. Meneveau, and J. Katz, On the properties of similarity subgrid-scale models as deduced from measurements in a turbulent jet, J. Fluid Mech. **275**, 83 (1994).
[33] J. Bardina, J. Ferziger, and W. Reynolds, Improved subgrid-scale models for large-eddy simulation, in *13th Fluid and Plasma Dynamics Conference* (1980), p. 1357.
[34] B. Vreman, B. Geurts, and H. Kuerten, On the formulation of the dynamic mixed subgrid-scale model, Phys. Fluids **6**, 4057 (1994).
[35] J. Bardina, Improved turbulence models based on large eddy simulation of homogeneous, incompressible, turbulent flows, Tech. Rep., 1 (1983).
[36] K. Horiuti, A new dynamic two-parameter mixed model for large-eddy simulation, Phys. Fluids **9**, 3443 (1997).
[37] F. Sarghini, U. Piomelli, and E. Balaras, Scale-similar models for large-eddy simulations, Phys. Fluids **11**, 1596 (1999).
[38] S. Singh and D. You, A dynamic global-coefficient mixed subgrid-scale model for large-eddy simulation of turbulent flows, Int. J. Heat Fluid Flow **42**, 94 (2013).
[39] B. W. Anderson and J. A. Domaradzki, A subgrid-scale model for large-eddy simulation based on the physics of interscale energy transfer in turbulence, Phys. Fluids **24**, 065104 (2012).
[40] J. A. Domaradzki, W. Liu, and M. E. Brachet, An analysis of subgrid-scale interactions in numerically simulated isotropic turbulence, Phys. Fluids A **5**, 1747 (1993).
[41] J. A. Domaradzki, W. Liu, C. Härtel, and L. Kleiser, Energy transfer in numerically simulated wall-bounded turbulent flows, Phys. Fluids **6**, 1583 (1994).
[42] R. M. Kerr, J. A. Domaradzki, and G. Barbier, Small-scale properties of nonlinear interactions and subgrid-scale energy transfer in isotropic turbulence, Phys. Fluids **8**, 197 (1996).
[43] J. Holmen, T. J. Hughes, A. A. Oberai, and G. N. Wells, Sensitivity of the scale partition for variational multiscale large-eddy simulation of channel flow, Phys. Fluids **16**, 824 (2004).
[44] T. Hughes, G. Wells, and A. Wray, Energy transfers and spectral eddy viscosity of homogeneous isotropic turbulence: Comparison of dynamic Smagorinsky and multiscale models over a range of discretizations, Phys. Fluids **16**, 4044 (2004).
[45] Y. Bazilevs, V. Calo, J. Cottrell, T. Hughes, A. Reali, and G. Scovazzi, Variational multiscale residual-based turbulence modeling for large eddy simulation of incompressible flows, Comput. Methods Appl. Mech. Eng. **197**, 173 (2007).
[46] Y. Zhou, Eddy damping, backscatter, and subgrid stresses in subgrid modeling of turbulence, Phys. Rev. A **43**, 7049 (1991).
[47] J. L. Lumley, The structure of inhomogeneous turbulent flows, in *Atmospheric Turbulence and Radio Propagation*, edited by A. M. Yaglom and V. I. Tatarski (Nauka, Moscow, 1967), pp. 166–178.
[48] G. Berkooz, P. Holmes, and J. L. Lumley, The proper orthogonal decomposition in the analysis of turbulent flows, Annu. Rev. Fluid Mech. **25**, 539 (1993).
[49] P. Holmes, *Turbulence, Coherent Structures, Dynamical Systems and Symmetry* (Cambridge University Press, 2012).
[50] N. Aubry, On the hidden beauty of the proper orthogonal decomposition, Theor. Comput. Fluid Dyn. **2**, 339 (1991).
[51] P. Moin and R. D. Moser, Characteristic-eddy decomposition of turbulence in a channel, J. Fluid Mech. **200**, 471 (1989).

[52] G. Berkooz, J. Elezgaray, P. Holmes, J. Lumley, and A. Poje, The proper orthogonal decomposition, wavelets and modal approaches to the dynamics of coherent structures, Appl. Sci. Res. **53**, 321 (1994).
[53] S. Sanghi and N. Aubry, Mode interaction models for near-wall turbulence, J. Fluid Mech. **247**, 455 (1993).
[54] P. J. Holmes, J. L. Lumley, G. Berkooz, J. C. Mattingly, and R. W. Wittenberg, Low-dimensional models of coherent structures in turbulence, Phys. Rep. **287**, 337 (1997).
[55] B. R. Noack, K. Afanasiev, M. Morzyński, G. Tadmor, and F. Thiele, A hierarchy of low-dimensional models for the transient and post-transient cylinder wake, J. Fluid Mech. **497**, 335 (2003).
[56] C. W. Rowley, Model reduction for fluids, using balanced proper orthogonal decomposition, Int. J. Bifurcation Chaos Appl. Sci. Eng. **15**, 997 (2005).
[57] V. Shinde, E. Longatte, F. Baj, Y. Hoarau, and M. Braza, A Galerkin-free model reduction approach for the Navier–Stokes equations, J. Comput. Phys. **309**, 148 (2016).
[58] V. Shinde, E. Longatte, F. Baj, Y. Hoarau, and M. Braza, Galerkin-free model reduction for fluid-structure interaction using proper orthogonal decomposition, J. Comput. Phys. **396**, 579 (2019).
[59] A. C. Poje and J. Lumley, A model for large-scale structures in turbulent shear flows, J. Fluid Mech. **285**, 349 (1995).
[60] M. Couplet, P. Sagaut, and C. Basdevant, Intermodal energy transfers in a proper orthogonal decomposition–Galerkin representation of a turbulent separated flow, J. Fluid Mech. **491**, 275 (2003).
[61] N. Aubry, W.-Y. Lian, and E. S. Titi, Preserving symmetries in the proper orthogonal decomposition, SIAM J. Sci. Comput. **14**, 483 (1993).
[62] K. Promislow, Time analyticity and Gevrey regularity for solutions of a class of dissipative partial differential equations, Nonlinear Anal. **16**, 959 (1991).
[63] H. Tennekes and J. Lumley, *A First Course in Turbulence* (MIT Press, 1972).
[64] C. Foias, O. Manley, and L. Sirovich, Empirical and Stokes eigenfunctions and the far-dissipative turbulent spectrum, Phys. Fluids A **2**, 464 (1990).
[65] R. H. Kraichnan, Inertial-range transfer in two- and three-dimensional turbulence, J. Fluid Mech. **47**, 525 (1971).
[66] R. H. Kraichnan, Eddy viscosity in two and three dimensions, J. Atmos. Sci. **33**, 1521 (1976).
[67] L. Sirovich, Turbulence and the dynamics of coherent structures. I. Coherent structures, Q. Appl. Math. **45**, 561 (1987).
[68] M. Germano, Turbulence: The filtering approach, J. Fluid Mech. **238**, 325 (1992).
[69] C. D. Pruett, Eulerian time-domain filtering for spatial large-eddy simulation, AIAA J. **38**, 1634 (2000).
[70] C. Pruett, T. Gatski, C. E. Grosch, and W. Thacker, The temporally filtered Navier–Stokes equations: Properties of the residual stress, Phys. Fluids **15**, 2127 (2003).
[71] U. Schumann, Realizability of Reynolds-stress turbulence models, Phys. Fluids **20**, 721 (1977).
[72] F. Archambeau, N. Méchitoua, and M. Sakiz, CODESATURNE: A finite volume code for the computation of turbulent incompressible flows-industrial applications, Int. J. Finite Volumes **1**, https://www.code-saturne.org/cms/ (2004).
[73] S. Benhamadouche and D. Laurence, LES, coarse LES, and transient RANS comparisons on the flow across a tube bundle, Int. J. Heat Fluid Flow **24**, 470 (2003).
[74] J. Crank and P. Nicolson, A practical method for numerical evaluation of solutions of partial differential equations of the heat-conduction type, Adv. Comput. Math. **6**, 207 (1996).
[75] H. K. Versteeg and W. Malalasekera, *An Introduction to Computational Fluid Dynamics: The Finite Volume Method* (Pearson Education, 2007).
[76] A. J. Chorin, Numerical solution of the Navier-Stokes equations, Math. Comput. **22**, 745 (1968).
[77] C. Rhie and W. L. Chow, Numerical study of the turbulent flow past an airfoil with trailing edge separation, AIAA J. **21**, 1525 (1983).
[78] S. Benhamadouche, Large eddy simulation with the unstructured collocated arrangement, Ph.D. thesis, The University of Manchester (United Kingdom), 2007.
[79] M. Antonopoulos-Domis, Aspects of large eddy simulation of homogeneous isotropic turbulence, Int. J. Numer. Methods Fluids **1**, 273 (1981).

[80] S. Biringen and W. Reynolds, Large-eddy simulation of the shear-free turbulent boundary layer, J. Fluid Mech. **103**, 53 (1981).
[81] T. Lund, The use of explicit filters in large eddy simulation, Comput. Math. Appl. **46**, 603 (2003).
[82] J. Gullbrand, Explicit filtering and subgrid-scale models in turbulent channel flow, Annual Research Briefs, 31 (2001).
[83] J. Gullbrand, Grid-independent large-eddy simulation in turbulent channel flow using three-dimensional explicit filtering, Annual Research Briefs, 331 (2003).
[84] L. Di Mare and W. Jones, LES of turbulent flow past a swept fence, Int. J. Heat Fluid Flow **24**, 606 (2003).
[85] S. Ghosal and P. Moin, The basic equations for the large eddy simulation of turbulent flows in complex geometry, J. Comput. Phys. **118**, 24 (1995).
[86] G. Comte-Bellot and S. Corrsin, Simple Eulerian time correlation of full-and narrow-band velocity signals in grid-generated, "isotropic" turbulence, J. Fluid Mech. **48**, 273 (1971).
[87] M. Lee and R. D. Moser, Direct numerical simulation of turbulent channel flow up to $Re_\tau \approx 5200$, J. Fluid Mech. **774**, 395 (2015).
[88] U. Piomelli, W. H. Cabot, P. Moin, and S. Lee, Subgrid-scale backscatter in turbulent and transitional flows, Phys. Fluids A **3**, 1766 (1991).
[89] C. Meneveau, Statistics of turbulence subgrid-scale stresses: Necessary conditions and experimental tests, Phys. Fluids **6**, 815 (1994).
[90] U. Piomelli, High Reynolds number calculations using the dynamic subgrid-scale stress model, Phys. Fluids A **5**, 1484 (1993).
[91] A. Misra and D. I. Pullin, A vortex-based subgrid stress model for large-eddy simulation, Phys. Fluids **9**, 2443 (1997).
[92] W. Rozema, H. J. Bae, P. Moin, and R. Verstappen, Minimum-dissipation models for large-eddy simulation, Phys. Fluids **27**, 085107 (2015).
[93] H. S. Kang, S. Chester, and C. Meneveau, Decaying turbulence in an active-grid-generated flow and comparisons with large-eddy simulation, J. Fluid Mech. **480**, 129 (2003).
[94] T. A. Oliver, N. Malaya, R. Ulerich, and R. D. Moser, Estimating uncertainties in statistics computed from direct numerical simulation, Phys. Fluids **26**, 035101 (2014).
[95] A. Vreman and J. G. Kuerten, Comparison of direct numerical simulation databases of turbulent channel flow at $Re_\tau = 180$, Phys. Fluids **26**, 015102 (2014).
[96] J. Kim, P. Moin, and R. Moser, Turbulence statistics in fully developed channel flow at low Reynolds number, J. Fluid Mech. **177**, 133 (1987).
[97] R. D. Moser, J. Kim, and N. N. Mansour, Direct numerical simulation of turbulent channel flow up to $Re_\tau = 590$, Phys. Fluids **11**, 943 (1999).
[98] A. Glezer, Z. Kadioglu, and A. J. Pearlstein, Development of an extended proper orthogonal decomposition and its application to a time periodically forced plane mixing layer, Phys. Fluids A **1**, 1363 (1989).
[99] E. A. Gillies, Low-dimensional characterization and control of non-linear wake flows, Ph.D. thesis, University of Glasgow, 1995.
[100] S. Siegel, K. Cohen, J. Seidel, and T. McLaughlin, Short time proper orthogonal decomposition for state estimation of transient flow fields, in *43rd AIAA Aerospace Sciences Meeting and Exhibit* (2005), p. 296.
[101] G. H. Golub and H. A. Van der Vorst, Eigenvalue computation in the 20th century, in *Numerical Analysis: Historical Developments in the 20th Century* (Elsevier, 2001), pp. 209–239.
[102] C. Pruett, Temporal large-eddy simulation: Theory and implementation, Theor. Comput. Fluid Dyn. **22**, 275 (2008).

Correction: Equations (5), (6), (8), and (10) were improperly manipulated during the production stage and have been fixed.